Supplementary Information (SI) for Journal of Materials Chemistry A.
This journal is © The Royal Society of Chemistry 2026

Electronic Supplementary Information

of

Enhancing the Valence Band Charge Localization via Zinc Doping into $MnWO_4$ to Promote Selective Ammonia Electrooxidation

Hirak Kumar Basak,[a] Bhawna Kamboj,[a] Jayanta Patra,[a] Dibyajyoti Ghosh,[a] [b] and Biswarup Chakraborty[a]*

[a] Department of Chemistry, Indian Institute of Technology Delhi, Hauz Khas, 110016, New Delhi, India

[b]Department of Materials Science and Engineering, Indian Institute of Technology Delhi, Hauz Khas, New Delhi, 110016, India

*Email id: cbiswarup@chemistry.iitd.ac.in

Table of Content

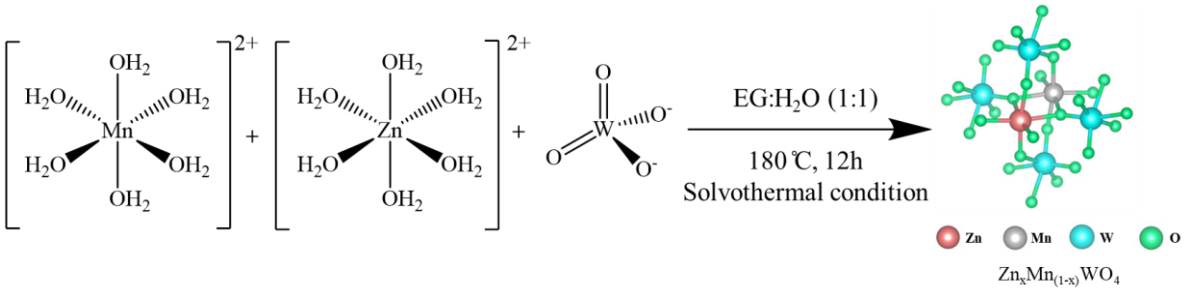

Scheme S1. Schematic representation of the synthesis of Zn-doped and undoped $MnWO_4$

Characterization and Analytical Techniques

Powder X-ray Diffraction (PXRD): The phase purity and crystalline structure of $Zn_xMn_{1-x}WO_4$.They were assessed using powder X-ray diffraction on a Bruker D8 Advance X-ray diffractometer equipped with Cu Kα X-ray tubes (λ = 1.5406 Å). The diffraction pattern was recorded in the 2θ range of 10° to 80° and compared with the respective ICDD (International Centre for Diffraction Data) data files for phase purity determination. Crystallite size was calculated using Scherrer's formula, Crystallite size (D) = $K\lambda/\beta\cos\theta$, where θ is the angle between incident and reflected X-rays, β is the full width at half maximum, λ is the X-ray wavelength, and K is the shape factor constant (K = 0.89).

Fourier Transform Infrared Spectroscopy (FTIR): FTIR analysis was conducted to identify bonding types and functional groups in the material. A KBr pellet containing the sample was prepared by mixing a small amount of the sample with KBr powder. The mixture was homogenized and pressed under hydraulic pressure to create a palette. FTIR measurements were performed using a Nicolet Protege 460 instrument.

Field Emission Scanning Electron Microscope (FESEM): FESEM was employed to study the microstructure of the synthesized nanomaterial. Energy dispersive X-ray spectroscopy (EDX) was also carried out for elemental analysis and mapping. These techniques were applied to samples deposited on NF before and after electrocatalysis using a JSM-IT300HR, JEOL instrument.

Transmission Electron Microscopy (TEM): Transmission electron microscopy, high-resolution TEM (HRTEM) imaging, and selected area electron diffraction (SAED) patterns were obtained using a JEOL HRTEM operating at an acceleration voltage of 200 kV. TEM grids were prepared using a dilute suspension of $Zn_{0.1}Mn_{0.9}WO_4$ in HPLC-grade ethanol on carbon-coated Cu grids.

X-ray Photoelectron Spectroscopy (XPS): Surface analysis of the synthesized material was conducted to determine the surface composition and oxidation states of chemical species using X-ray photoelectron spectroscopy (XPS). Measurements were performed using an ESCA+ instrument from Omicron Nanotechnology, Oxford Instrument Germany, equipped with an aluminum monochromator and aluminum source (Al Kα radiation hν = 1486.7 eV). The instrument operated at 15 kV and 15 mA.

Inductively coupled plasma mass spectrometry (ICP-OES): The chemical composition of the materials was analyzed using inductively coupled plasma optical emission spectroscopy (ICP-OES) with an Agilent 5110 instrument operated through ICP Expert software.

Spectrophotometric measurement (UV-VIS): All the optical spectra have been recorded using a dual beam Agilent Cary 60 spectrophotometer equipped with a Xenon flash lamp (80 Hz) ranging from 190 nm to 1100 nm. All the spectra have been recorded at a medium scanning rate.

Electrode fabrication. The powder materials were deposited on the 1 cm^2 surface area of the Ni foam. Before deposition of the materials to the NF surface, NF was cut into 2×1 cm pieces and then washed with dilute hydrochloric acid (0.1 M), Milli-Q water, and acetone through sonication for 10 minutes and then dried at 60 ° C.[1] The Nafion solution was diluted with ethanol to 1.0 wt% and 7-8 mg $MnWO_4$ or $Zn_xMn_{(1-x)}WO_4$ was added to 200 µl of the diluted Nafion solution. The resulting mixture was ultrasonicated for 30 minutes. The catalyst ink was then dropcasted through a micro-pipette on a 1 cm^2 NF surface.

Gas chromatography (GC): All gaseous products generated during the ammonia oxidation reaction (AOR) were analyzed using an Agilent 8860 GC system equipped with a thermal conductivity detector (TCD), with data acquisition and processing carried out via OpenLab CDS software. Argon was used as the carrier gas at a constant flow rate of 7.5 mL min^{-1}. The oven temperature was programmed to increase from 40°C to 120°C at a ramp rate of 10°C min^{-1}.

Electrode Kinetics measurement (RRDE experiment):

Calculation of the Number of electrons transferred (n) and observed rate constant (k_{obs}) during AOR from the RRDE study: From Figure 5g, h, using the K-L relation, the number of electrons transferred has been calculated from the slope of the graph between $1/i_L$ and $\omega^{-1/2}$.

$1515.3 \text{ (Slope)} = 1/[0.62\times n\times 96485.3\times \Pi\times (0.25)^2\times (1.2\times 10^{-5})^{2/3}\times (1.12\times 10^{-2})^{1/6}\times 25\times 10^{-6}]$

$n = 1/[0.62\times 1515.3\times 96485\times 0.1963\times (1.2\times 10^{-5})^{2/3}\times (1.12\times 10^{-2})^{1/6}\times 25\times 10^{-6}]$

$n = 1.989.$

Putting 'n' in equation 2 and using the intercept of the K-L plot, the observed rate constant of the electron transfer kinetics (k_{obs}) has been estimated.

$i_k = nFAk_{obs}C_0$

$163.89= 1.989\times 96485.3\times \Pi\times (0.25)^2\times 25\times 10^{-6}\times k_{obs.}$

$k_{obs}= 6.482\times 10^{-3}\ mol^{-1}cm^{-2}s^{-1}.$

*For more information about K-L analysis at different applied potentials, please refer to ***Table S5.***

Computational Methodology

We employed the Vienna Ab Initio Simulation Package (VASP) for all spin-polarised density functional theory calculations. The exchange-correlation interactions are treated within the generalised gradient approximation (GGA) formulated by Perdew–Burke–and Ernzerhof (PBE) functional. .[2-4] The computational framework utilized projected augmented wave pseudopotentials with scalar relativistic treatments and a 420 eV plane-wave energy cutoff [5, 6] To accurately describe the strongly correlated d-electrons in transition metal oxides, the DFT+U approach is implemented.[3] Structural optimizations are carried out for both pristine and Zn-doped $MnWO_4$ systems until the interatomic Hellmann-Feynman forces converge below 0.01 eV/Å. The Brillouin zone sampling utilizes Γ-centered Monkhorst-Pack k-point meshes of 3×2×2 for structural optimization and 5×4×2 for self-consistent field (SCF) calculations, respectively.[7] To model Zn substitution at 6.25%, 12.5%, and 18.75% concentrations in $Zn_xMn_{(1-x)}WO_4$, a 2×2×2 supercell of the primitive $MnWO_4$ structure is constructed. The dopant configurations are systematically chosen to maximize spatial separation between Zn atoms and minimize dopant-dopant interactions, as illustrated in Figure 1a. The SUMO command-line tool determines the hole effective masses by fitting parabolic functions to the valence band maximum (VBM) dispersion.[8]

Calculations of Chemical Potential:

Chemical potentials for 'Zn' and 'Mn' are calculated from their respective bulk structures obtained from the OQMD database.[9] The chemical potentials are referenced to well-defined states according to:

$$\mu_i = \mu_i^0 + \Delta\mu_i$$

Where μ_i^0 represents the fixed reference state, and $\Delta\mu_i$ is the relative chemical potential for the specific conditions. We use the standard reference state for each element (the stable phase under standard conditions) and obtain reference energies directly from DFT total energies per atom at 0 K, neglecting temperature and pressure effects.

Synthesis and characterization of $Zn_xMn_{1-x}WO_4$.

Table S1. ICP-MS study of the synthesized 5, 10, 15% Zn-doped $MnWO_4$ materials.

		55 Mn [Ar]		65.4 Zn [Ar]		184 W [Ar]	
Type	Sample Name	Conc. [ppm]	Conc. RSD	Conc. [ppm]	Conc. RSD	Conc. [ppm]	Conc. RSD
CalBlk	BLANK	0	N/A	0	N/A	0	N/A
CalStd	1 ppm	1.03	3.06	0.97	3.06	0.97	3.06
CalStd	2 ppm	2.02	1.05	2.01	0.69	2.01	0.69
CalStd	5 ppm	4.95	1.00	5.02	0.35	5.02	0.35
CalStd	6 ppm	5.90	1.73	6.06	1.05	6.06	1.05
Sample[a]	5%Zn-$MnWO_4$	0.96	0.58	0.06	0.81	0.97	1.68
Sample[a]	10%Zn-$MnWO_4$	0.69	0.19	0.09	1.15	0.72	2.53
Sample[a]	15%Zn-$MnWO_4$	0.93	0.93	0.18	0.24	0.49	1.40

[a]The solid samples were digested using aqua regia and liquid samples were diluted 100 times before the experiment.

Table S2. ICP-MS study of the synthesized 5, 10, 15% Zn-doped $MnWO_4$ materials.

Sample-1 (5% Zn doped $MnWO_4$)	Mn	Zn
Experimental ratio (molar)	95	5
ICP-MS data (in ppm)	0.96	0.06
ICP-MS data (in M)	1.74736×10^{-5}	9.17712×10^{-7}
Molar ratio	95.01	4.99
Empirical formula	**$Zn_{0.05}Mn_{0.95}WO_4$**	
Sample-2 (10% Zn-doped $MnWO_4$)	Mn	Zn
Experimental ratio (molar)	90	10
ICP-MS data (in ppm)	0.69	0.09
ICP-MS data (in M)	1.25592×10^{-5}	1.37657×10^{-6}
Molar ratio	90.12	9.88
Empirical formula	**$Zn_{0.1}Mn_{0.9}WO_4$**	
Sample-3 (15% Zn doped $MnWO_4$)	Ni	Zn
Experimental ratio (molar)	85	15
ICP-MS data (in ppm)	0.93	0.18
ICP-MS data (in M)	1.6927×10^{-5}	2.75314×10^{-6}
Molar ratio	86.01	13.98
Empirical formula	**$Zn_{0.14}Mn_{0.86}WO_4$**	

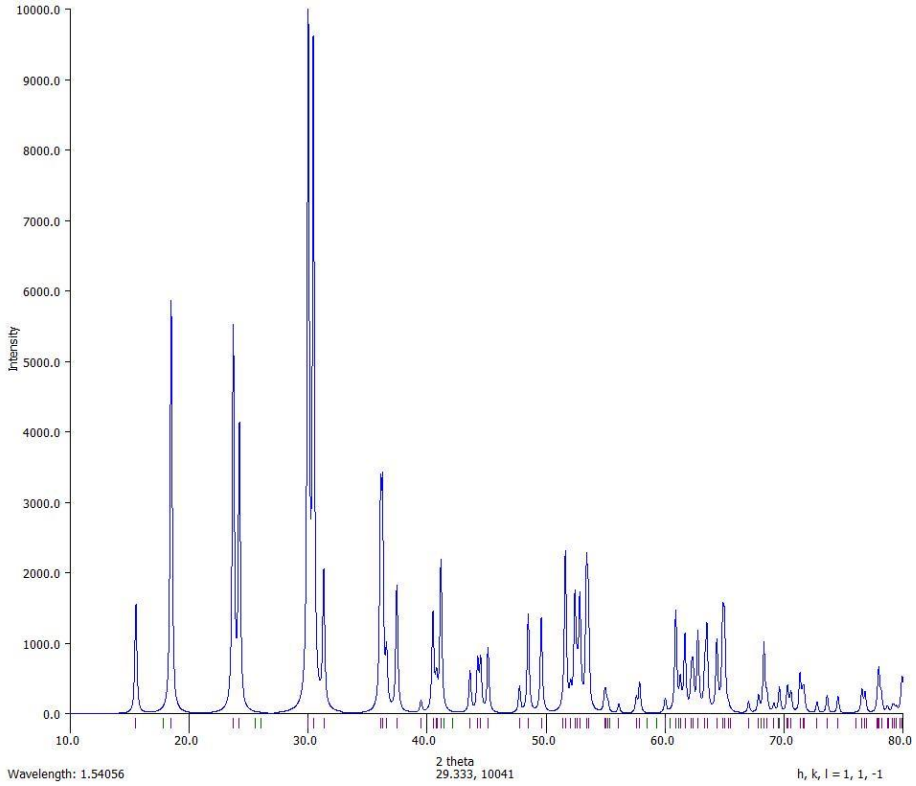

Figure S1. PXRD obtained from the .cif file used for the representative figure for $MnWO_4$, which is well correlated to the obtained PXRD pattern of synthesized doped and undoped $MnWO_4$, along with the ICDD card number 00-013-0434.

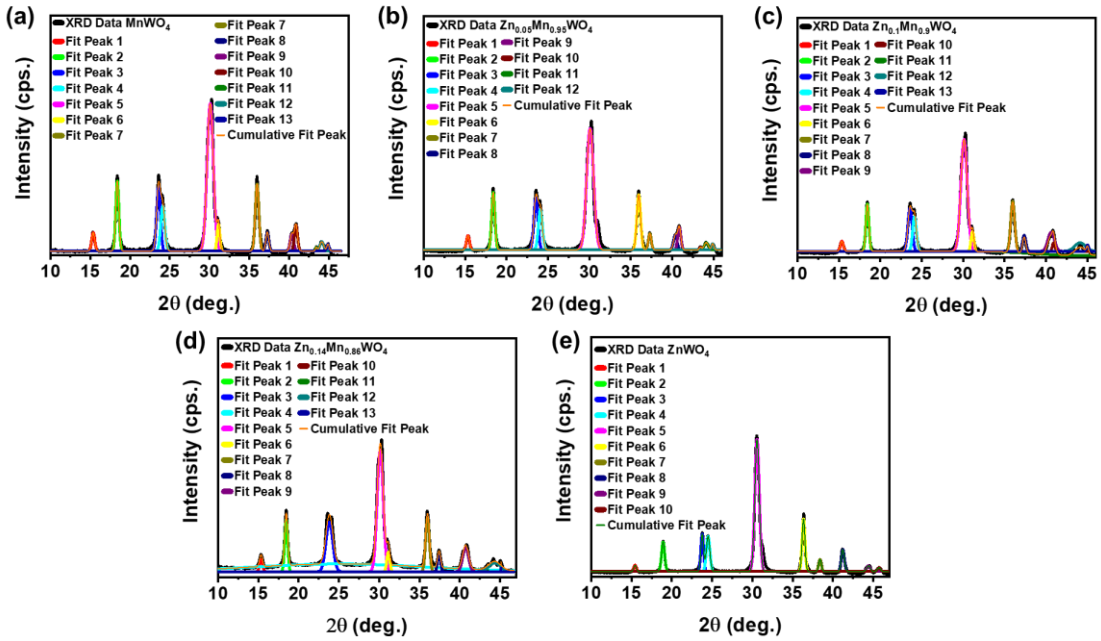

Figure S2. Crystallite size determination from PXRD. Fitted PXRD spectra of (a) $MnWO_4$, (b) $Zn_{0.05}Mn_{0.95}WO_4$, (c) $Zn_{0.1}Mn_{0.9}WO_4$, (d) $Zn_{0.14}Mn_{0.86}WO_4$, and (e) $ZnWO_4$.

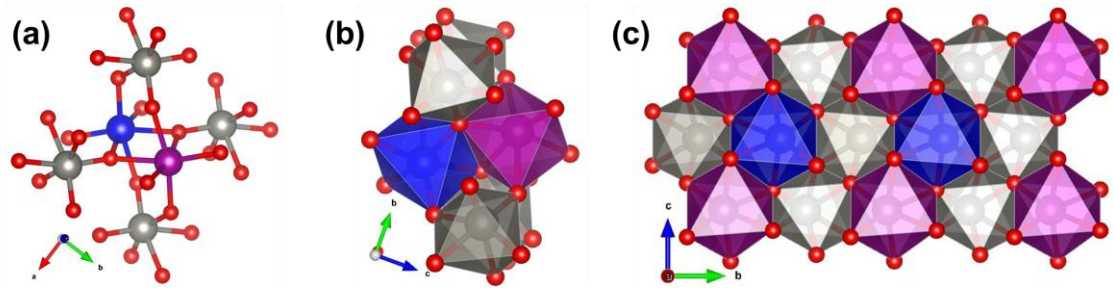

Figure S3. 3-D lattice view of Zn-doped $MnWO_4$. (a) Ball stick model structure of Zn-doped $MnWO_4$, (blue sphere: zinc atom, magenta sphere: manganese atom, grey sphere: tungsten atom, and red spheres: oxygen atom). (b) Polyhedral model structure of Zn-doped $MnWO_4$, Color code: ZnO_6 (Blue), MnO_6 (magenta), and WO_6 (grey) octahedra, edge, and corner-sharing of ZnO_6, MnO_6, WO_6 octahedra. (c) Extended lattice view of Zn-doped $MnWO_4$.

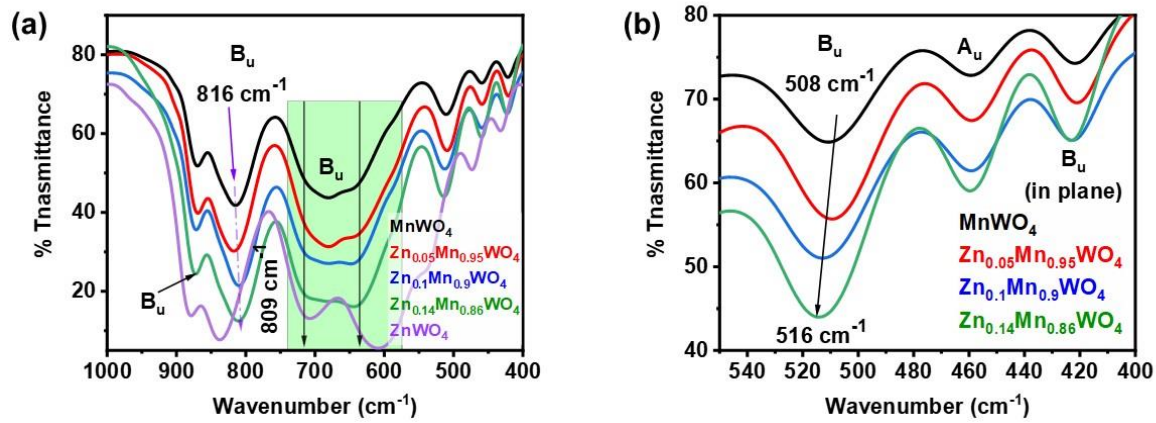

Figure S4. FTIR spectra of $MnWO_4$ and Zn-doped $MnWO_4$ nanomaterials within (a) 400-1000 cm^{-1} and (b) 400-550 cm^{-1} region.[10]

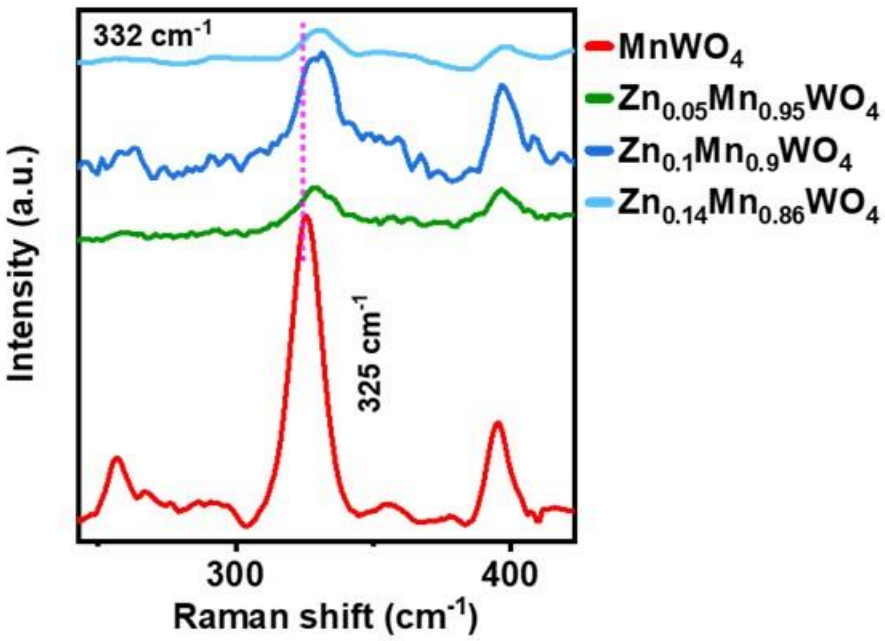

Figure S5. FTIR spectra of $MnWO_4$ and Zn-doped $MnWO_4$ nanomaterials within (a) 400-1000 cm^{-1} and (b) 400-550 cm^{-1} region.[11]

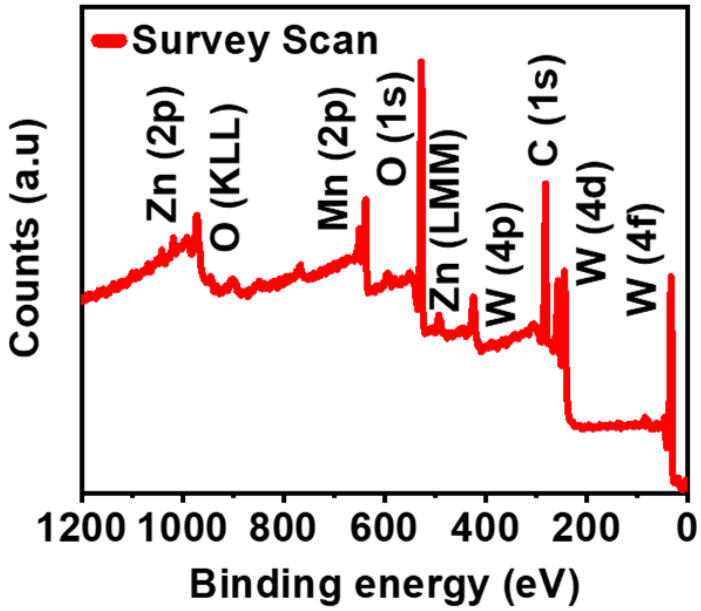

Figure S6. XPS survey spectrum of the as-synthesized $Zn_{0.1}Mn_{0.9}WO_4$ nanoparticles confirming the presence of Zn, Mn, W, and O.

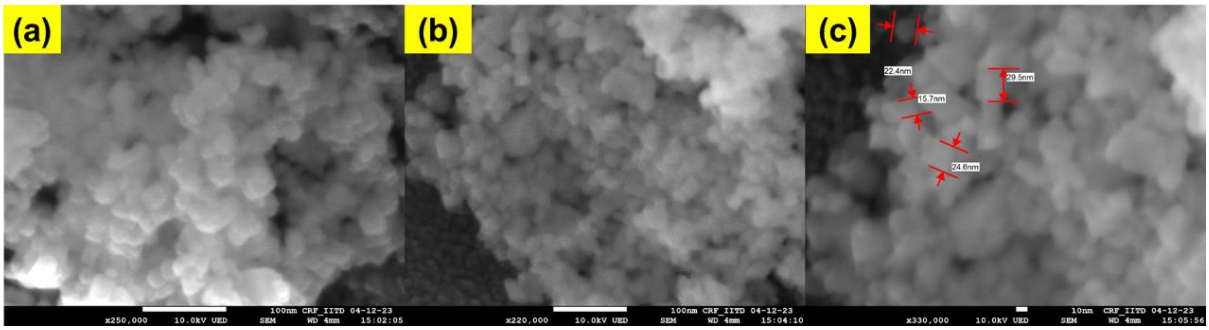

Figure S7. (a-c) Additional FE-SEM image of as-synthesized $Zn_{0.1}Mn_{0.9}WO_4$ at different magnifications.

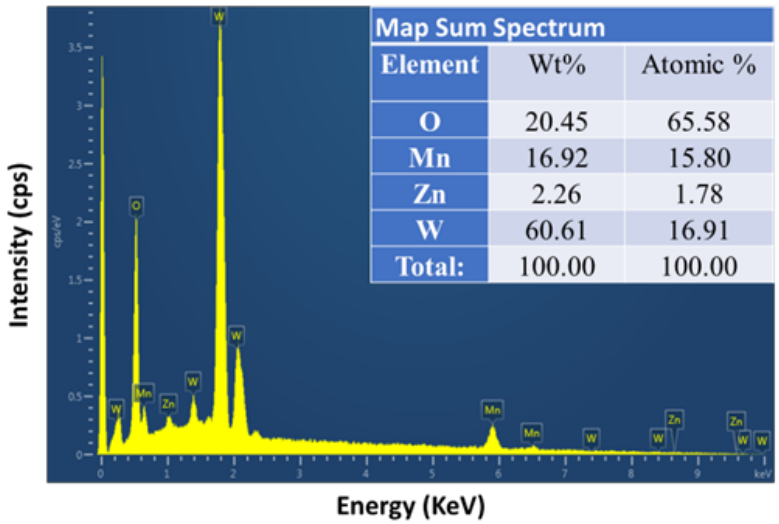

Figure S8. FESEM-EDX spectrum of as-synthesized $Zn_{0.1}Mn_{0.9}WO_4$.

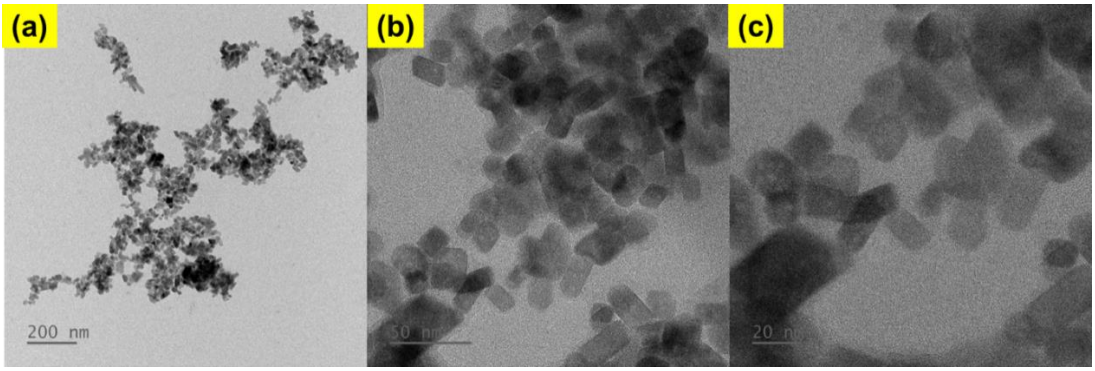

Figure S9. (a-c) Additional TEM image at different magnifications of $Zn_{0.1}Mn_{0.9}WO_4$.

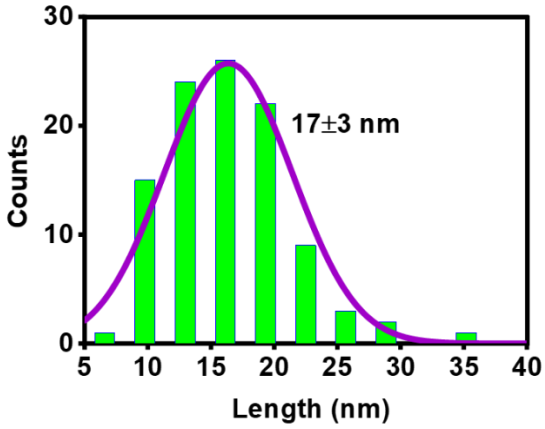

Figure S10. Particle size distribution of $Zn_{0.1}Mn_{0.9}WO_4$ materials obtained from the TEM image, considering 100 nanoparticles.

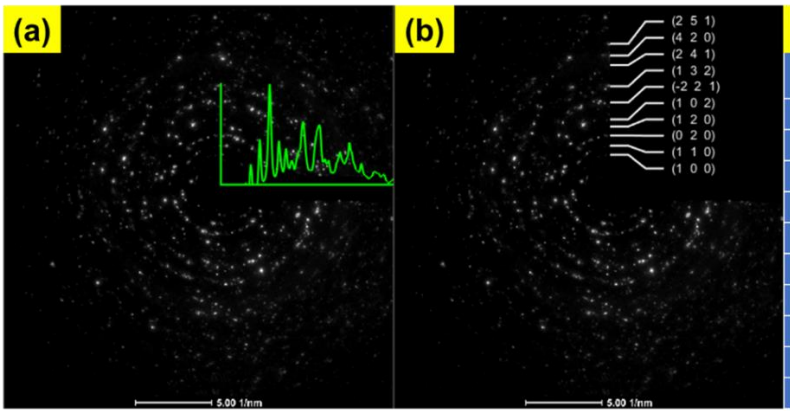

(c)

Ring identification				
Plane	Radius [1/nm]		d-spacing [nm]	
	theor.	measured	theor.	measured
(1 0 0)	2.091	2.098	0.478	0.477
(1 1 0)	2.720	2.733	0.368	0.366
(0 2 0)	3.478	3.450	0.288	0.290
(1 2 0)	4.058	4.085	0.246	0.245
(1 0 2)	4.548	4.582	0.220	0.218
(-2 2 1)	5.768	5.769	0.173	0.173
(1 3 2)	6.921	6.901	0.144	0.145
(2 4 1)	8.378	8.391	0.119	0.119
(4 2 0)	9.059	9.054	0.110	0.110
(2 5 1)	9.869	9.882	0.101	0.101

Figure S11. SAED analysis of $Zn_{0.1}Mn_{0.9}WO_4$ and correlation to the plane corresponding to each diffraction ring. (a) SAED and convoluted 1D intensity profile. (b) indexed plane for each diffraction ring in SAED. (c) Theoretical and measured distance correlation of radius in reciprocal space (1/nm) and d-spacing (nm).

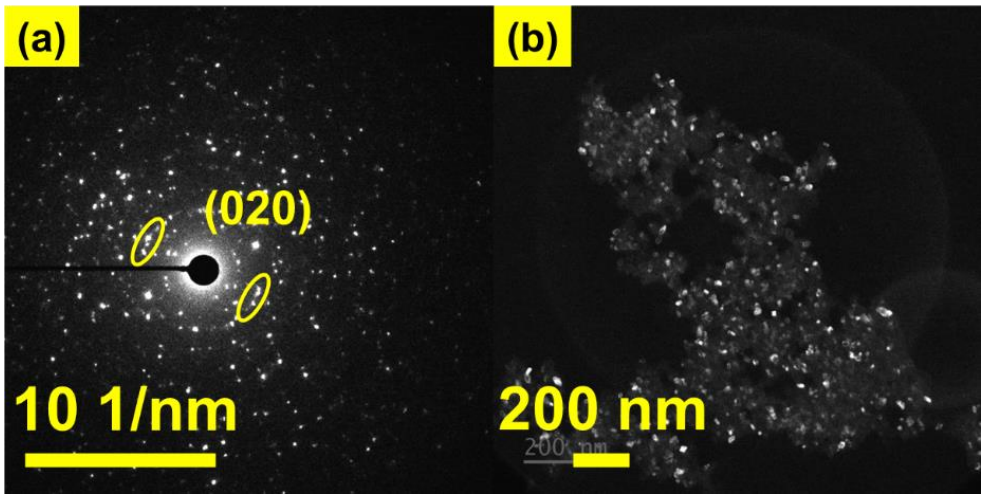

Figure S12. (a) SAED pattern of the diffracted beam, (b) exposed facet of the (020) plane in dark-field HR-TEM of as-synthesized $Zn_{0.1}Mn_{0.9}WO_4$.

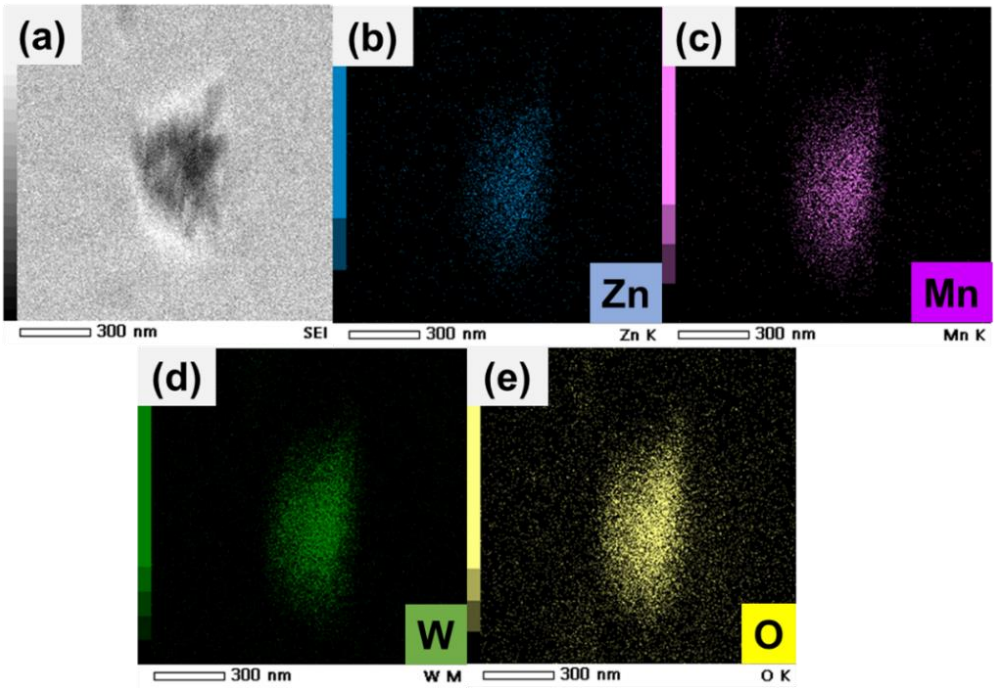

Figure S13. (a) HR-TEM image of $Zn_{0.1}Mn_{0.9}WO_4$ material and corresponding elemental mapping for (b) Zn, (c) Mn, (d) W, and (e) O s.

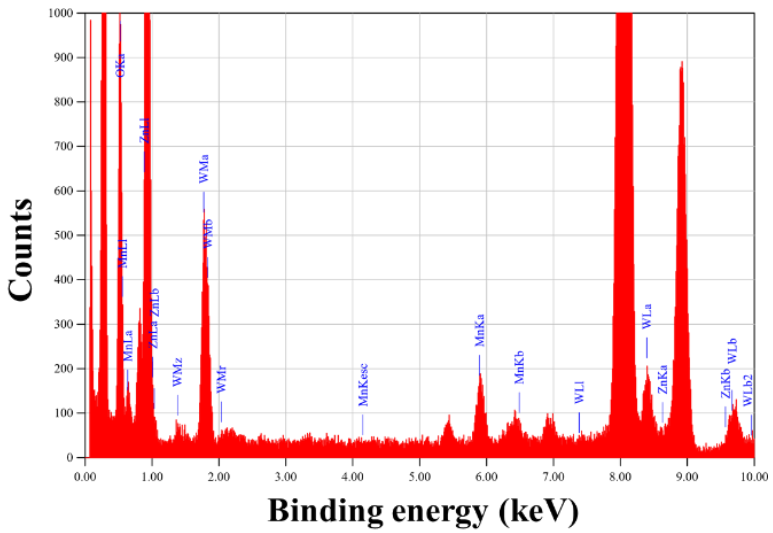

Figure S14. TEM-EDX spectrum of $Zn_{0.1}Mn_{0.9}WO_4$ indicating the presence of Zn, Mn, W, and O.

Table S3. Quantitative analysis of the TEM-EDX spectrum of $Zn_{0.1}Mn_{0.9}WO_4$.

Element	(keV)	Mass%	Atom%
O K	0.525	37.32	81.48
Mn K	5.894	12.03	7.65
Zn K	8.630	3.61	1.03
W M	1.774	47.05	8.94
Total		100.00	100.00

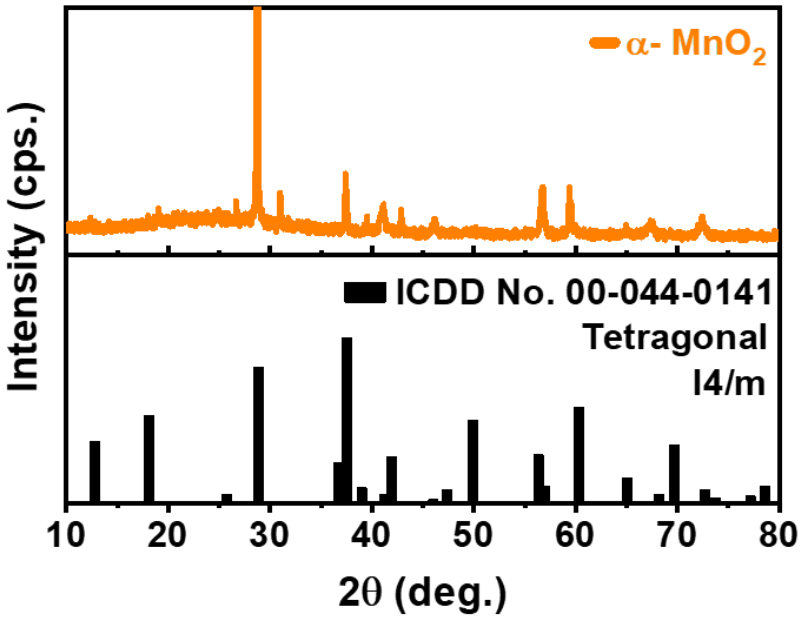

Figure S15. (a) PXRD pattern of α-MnO_2 and the standard diffraction pattern for ICDD card No. 00-044-0141.

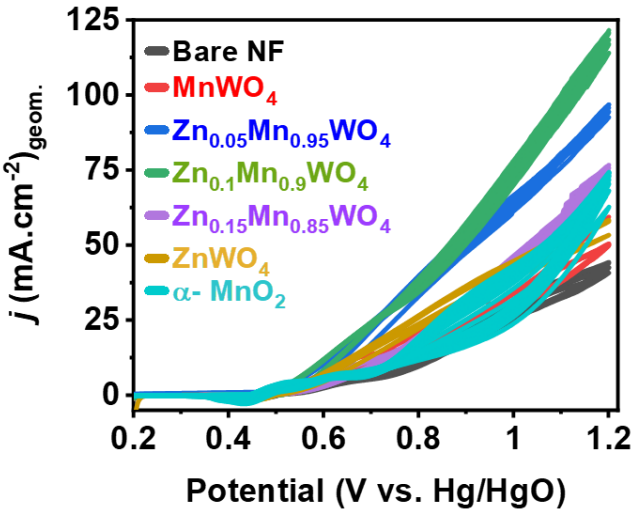

Figure S16. Electrochemical AOR study using Blank-NF, $MnWO_4$/NF, $Zn_{0.05}Mn_{0.95}WO_4$/NF, $Zn_{0.1}Mn_{0.9}WO_4$/NF, $Zn_{0.15}Mn_{0.85}WO_4$/NF, $ZnWO_4$/NF using 0.5 M NH_3 in 0.5 M NaOH. Polarization curves were obtained from the CV study using 0.5 M NH_3 in 0.5 M NaOH.

Table S4. Literature survey on heterogeneous electrocatalytic AOR catalysts and their performances.

Material	Substrate	NH_3 (Conc.)	Electrolyte	Onset (V)	Products (FE %)	Reference
$Zn_{0.1}Mn_{0.9}WO_4$	NF	0.5 M	0.5 M Na_2SO_4	0.62	$[NO_3]^-$ (70±5), $[NO_2]^-$(10±2)	This Work
$Zn_{0.05}Mn_{0.95}WO_4$	NF	0.5 M	0.5 M Na_2SO_4	0.68	$[NO_3]^-$ (60±5), $[NO_2]^-$(20±4)	This Work
$MnWO_4$	NF	0.5 M	0.5 M Na_2SO_4	~0.90	$[NO_3]^-$ (30±5),	This Work

					$[NO_2]^-$(5±2)	
NiOOH	NF	0.2 M	0.2 M K_2SO_4	0.6 V[a]	$[NO_2]^-$ $[NO_3]^-$ N_2	12
NiOOH-Ni	NF	0.2 M	0.1 M K_2SO_4	1.3 V[b]	$[NO_2]^-$ (90.4)	13
AgOx	Pt/Ti	0.1 M	0.1 M KOH	0.8 V[c]	$[NO_2]^-$ (70±6)	14
4%Pt/$NiWO_4$	NF	1 M	0.5 M NaOH	0.47 V[d]	$[NO_2]^-$(55) $[NO_3]^-$(30)	15
NF	-	1 M	0.5 M NaOH	0.60 V[d]	N_2 (22)	1
CoO_xH_y/β-NiOOH	NF	0.5 M	0.1 M K_2HPO_4	0.8 V[c]	$[NO_3]^-$ (50) $[NO_2]^-$ (27)	16
$Ni(OH)_2$/NiOOH	NF	0.2 M	0.1 M Na_2SO_4	1.5 V[b]	$[NO_3]^-$ (60) $[NO_2]^-$ (28)	17
0.12CeO_x /Y-400		NH_3 saturated	0.05 M $C_6H_9NO_3S$	0.69[b]	N_2	18
$NiCu/MnO_2$	CP	55 mM NH_4Cl	0.5 M NaOH	0.6 V[d]	N_2 (97)	19
$Ni(OH)_2$-Cu_2O@CuO	NF	1 M NH_3	1 M KOH	0.5-0.6 V[d]	N_2	20
$Cu_{(1-x)}Co_xOOH$	NF	0.01 M NH_3	0.1 M Na_2SO_4	0.6 V[a]	$[NO_3]^-$ (70±5) $[NO_2]^-$ (2)	21
Ni metal	NF	0.1 M NH_3	0.1 M KOH	1.7 V[b]	$[NO_3]^-$ (19±7) $[NO_2]^-$(8±2)	22
CeO_2 modified Pt	GC	0.1 M NH_3	1 M KOH	0.6 V[b]	N_2	23
Cu	-	0.1 M NH_3	0.1 M KOH	2.0 V[b]	$[NO_3]^-$ (18±5)	24
Co		0.1 M NH_3	0.1 M KOH	2.0 V[b]	$[NO_3]^-$ (17±3)	24
Fe		0.1 M NH_3	0.1 M KOH	2.0 V[b]	$[NO_3]^-$ (5.8±0.1)	24

[a](vs. Ag/AgCl), [b](vs. RHE), [c](vs. SHE), [d](vs. Hg/HgO); [NF] nickel foam; [GC] glassy carbon; [CP] Carbon paper.

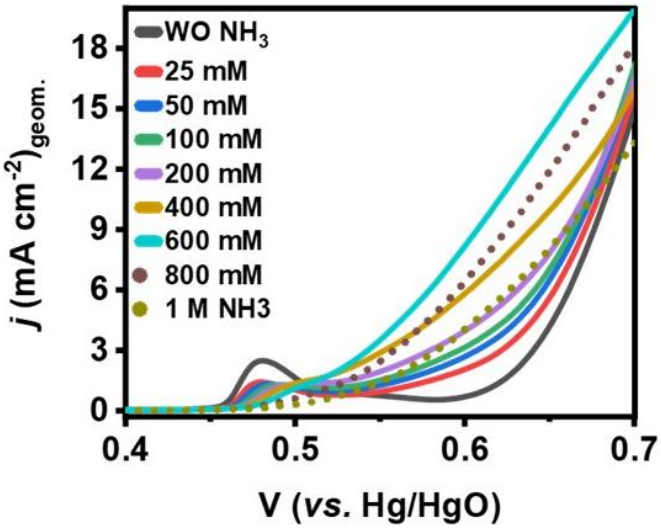

Figure S17. A linear sweep voltammogram (LSV) recorded with $Zn_{0.1}Mn_{0.9}WO_4$/NF electrode at a scan rate of 2 mV s^{-1}, varying ammonia concentrations in 0.5 M NaOH.

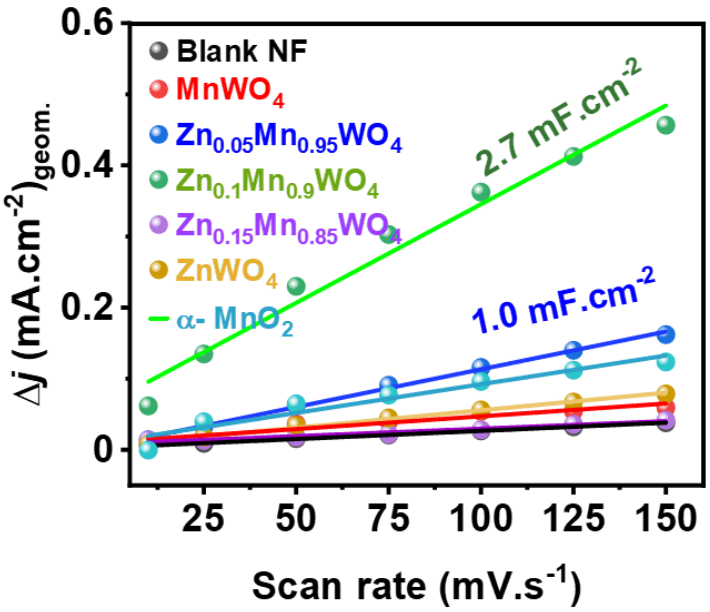

Figure S18. Double-layer capacitance during electrochemical AOR study using Blank-NF, $MnWO_4$/NF, $Zn_{0.05}Mn_{0.95}WO_4$/NF, $Zn_{0.1}Mn_{0.9}WO_4$/NF, $Zn_{0.15}Mn_{0.85}WO_4$/NF, $ZnWO_4$/NF in a mixture of 0.5 M NH_3 and 0.5 M NaOH.

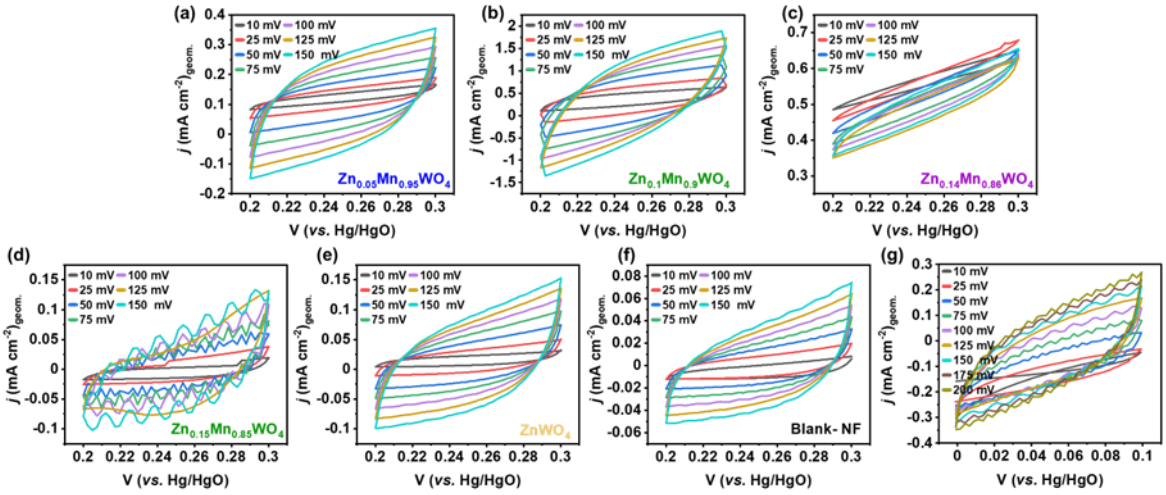

Figure S19. CV cycles at different scan rates with (a) $Zn_{0.05}Mn_{0.95}WO_4$, (b) $Zn_{0.1}Mn_{0.9}WO_4$, (c) $Zn_{0.14}Mn_{0.86}WO_4$, (d) $MnWO_4$, (e) $ZnWO_4$, (f) bare nickel foam (NF), and (f) α-MnO_2 in 0.5 M NH_3 containing 0.5 M NaOH solution. The potential range: 0.2 V to 0.3 V (vs. Hg/HgO) and sweep rates: 10 to 150 mV/s.

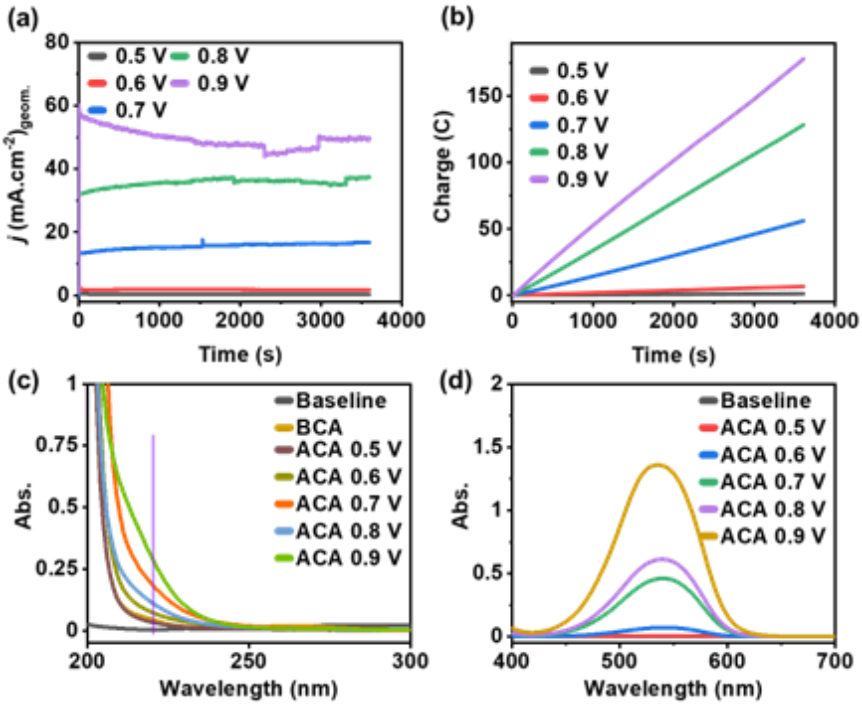

Figure S20. AOR in 0.5 M NH_3 containing 0.5 M NaOH using $Zn_{0.1}Mn_{0.9}WO_4$/NF electrode at different applied potentials and quantification of NO_x product via optical spectroscopy. (a) Current vs. time plot during bulk electrolysis stydy at five different potential, (b) corresponding time vs. charge plots. UV-vis absorption spectra obtained after 1 h bulk electrolysis at various potentials for (c) nitrate ($[NO_3]^-$), (d) nitrate ($[NO_2]^-$). (BCA: before CA-AOR and ACA: after CA-AOR)

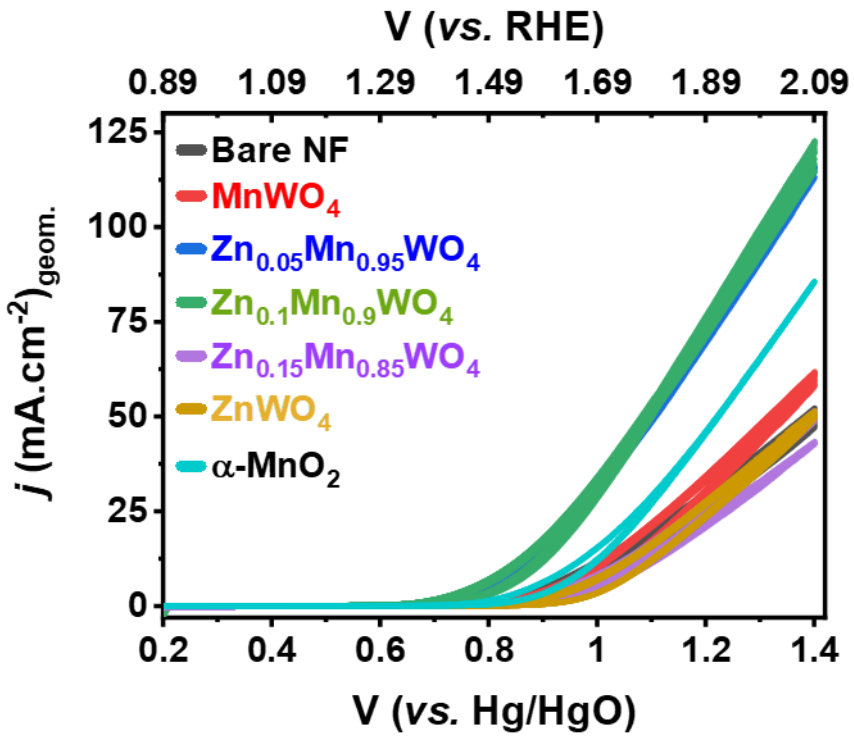

Figure S21. CV study for the electrochemical AOR using Blank-NF, $MnWO_4$/NF, $Zn_{0.05}Mn_{0.95}WO_4$/NF, $Zn_{0.1}Mn_{0.9}WO_4$/NF, $Zn_{0.15}Mn_{0.85}WO_4$/NF, $ZnWO_4$/NF, and α-MnO_2/NF in 0.5 M NH_3 in 0.5 M $NaSO_4$ electrolyte.

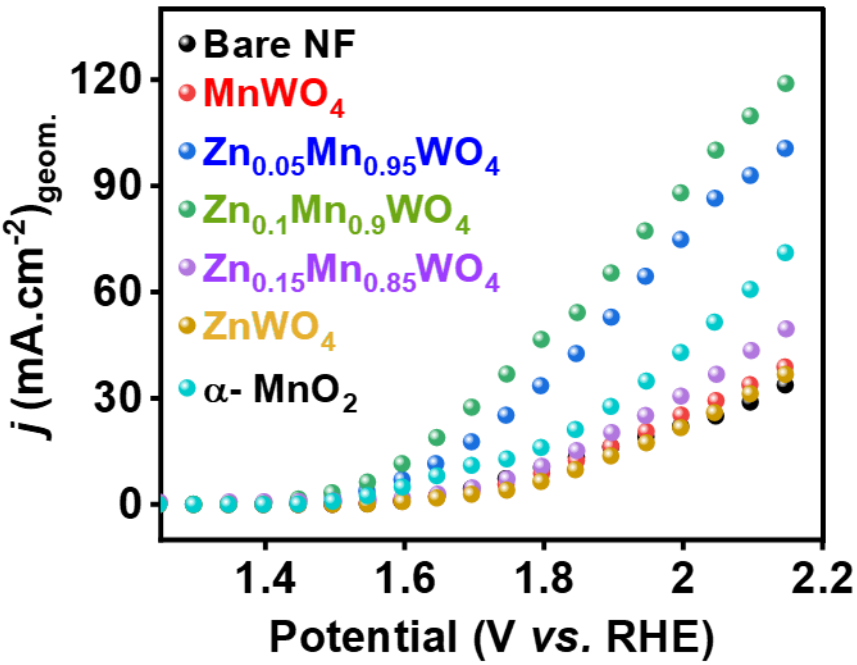

Figure S22. LSV plot derived from the steady state electrochemical CA-AOR (provided in the Figure S26) using blank-NF, $MnWO_4$/NF, $Zn_{0.05}Mn_{0.95}WO_4$/NF, $Zn_{0.1}Mn_{0.9}WO_4$/NF, $Zn_{0.15}Mn_{0.85}WO_4$/NF, $ZnWO_4$/NF, and α-MnO_2/NF in 0.5 M NH_3 in 0.5 M $NaSO_4$ electrolyte.

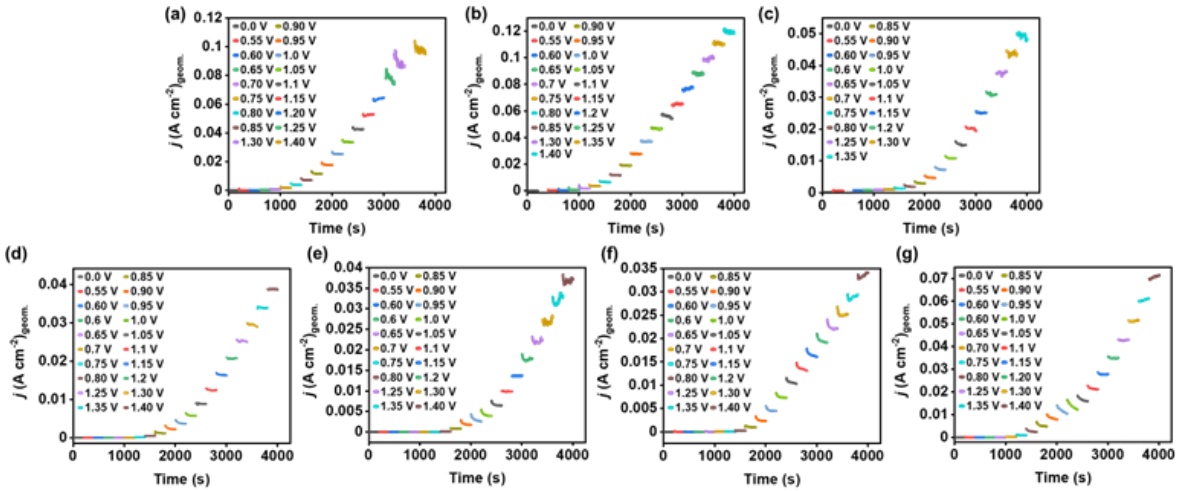

Figure S23. Current versus time plots obtained from the chronoamperometry studies in electrolyte using (a) $Zn_{0.05}Mn_{0.95}WO_4$/NF, (b) $Zn_{0.1}Mn_{0.9}WO_4$/NF, (c) $MnWO_4$/NF, (d) $Zn_{0.15}Mn_{0.85}WO_4$/NF, (e) $ZnWO_4$/NF, (f) blank-NF AOR, and (g) α-MnO_2/NF. (Inset: the values of applied potential for the CA study).

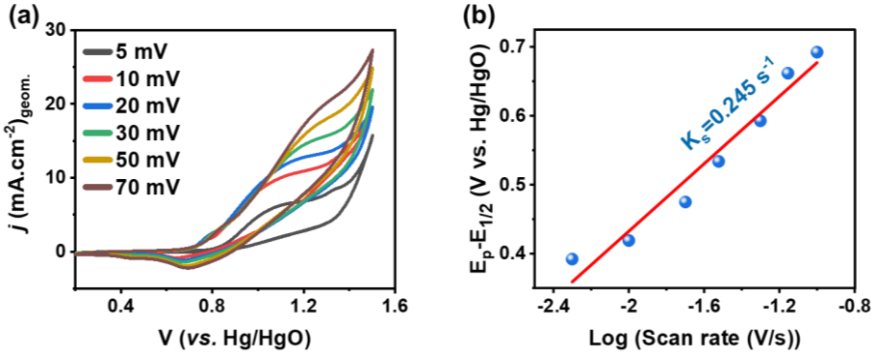

Figure S24. (a) Cyclic voltammogram (CV) recorded varying scan rate from 5 to 70 mV s^{-1} in 0.5 M Na_2SO_4 containing 0.5 M NH_3 using $Zn_{0.1}Mn_{0.9}WO_4$/NF electrode, (b) corresponding redox peak potentials versus the logarithmic scan rates plot to determine rate of AOR by using Laviron equation.[25]

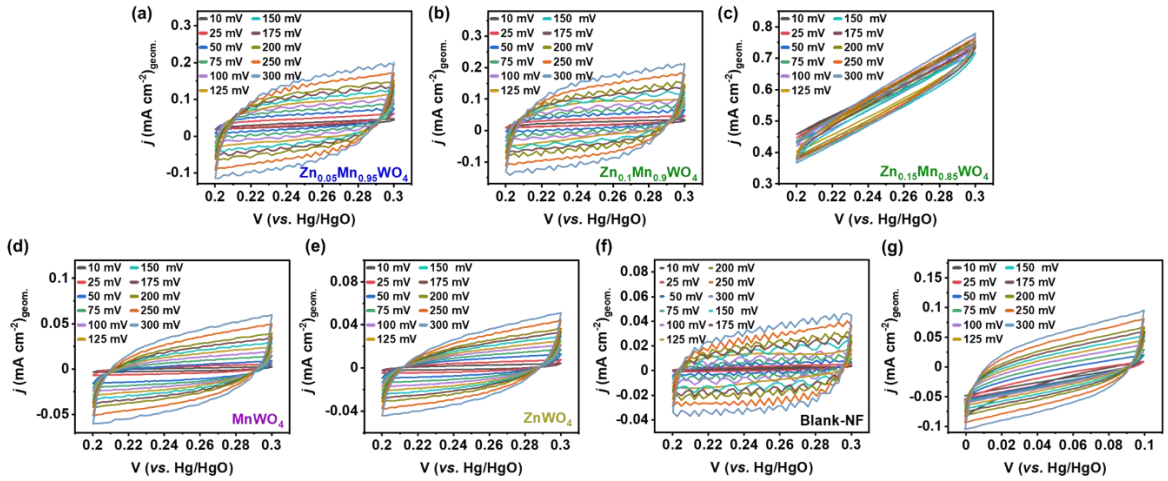

Figure S25. CV cycles recorded at different scan rates using (a) $Zn_{0.05}Mn_{0.95}WO_4$/NF, (b) $Zn_{0.1}Mn_{0.9}WO_4$/NF, (c) $Zn_{0.14}Mn_{0.86}WO_4$/NF, (d) $MnWO_4$/NF, (e) $ZnWO_4$/NF, (f) bare nickel foam (NF), and (g) α-MnO_2/NF in 0.5 M NH_3 containing 0.5 M Na_2SO_4 solution.

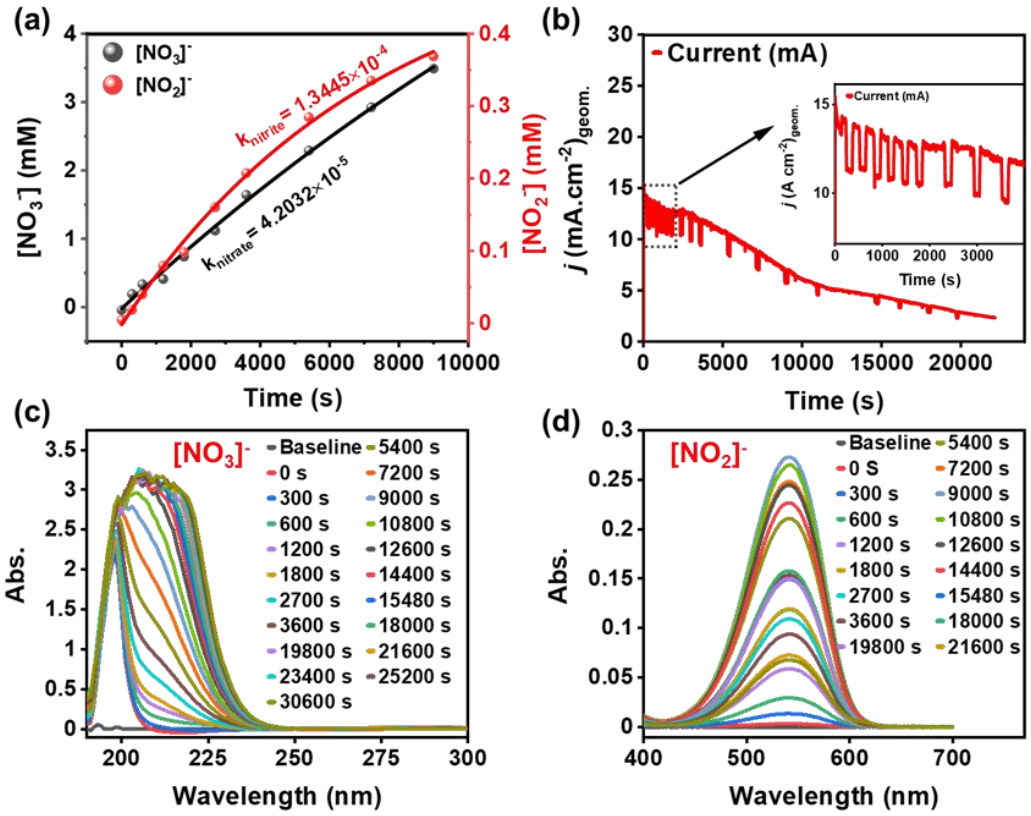

Figure S26. (a) Concentration versus time profile for 8500 s for the nitrate and nitrite concentration obtained during 10 h CA study at 1.0 V (vs. Hg/HgO). (b) Current versus time profile obtained during the constant 1.0 V (vs. Hg/HgO) applied potential electrolysis for AOR. Quasi in situ UV-vis absorption spectra of (c) nitrate and (d) nitrite formed in the electrolyte obtained at different time intervals during AOR.

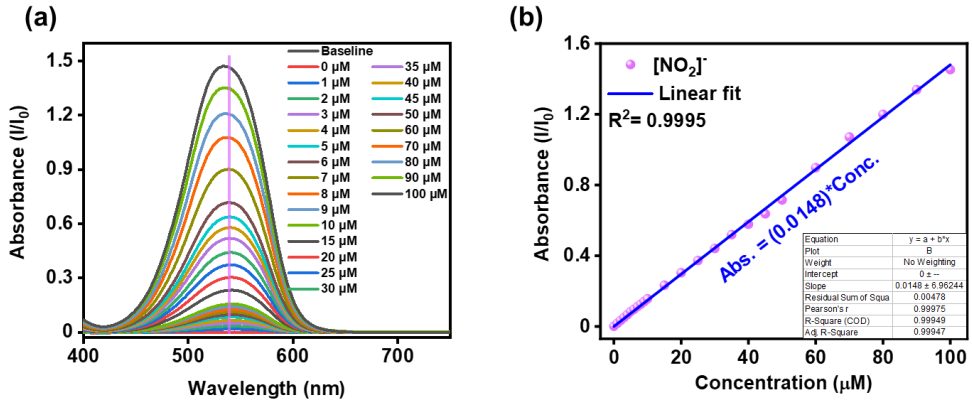

Figure S27. Calibration curves made with different concentrations of nitrite. (a) Electronic spectra of 0 to 100 µM of nitrite and (b) absorbance vs. concentration plot at the λ_{max} of 541 nm wavelength of $[NO_2]^-$.[26]

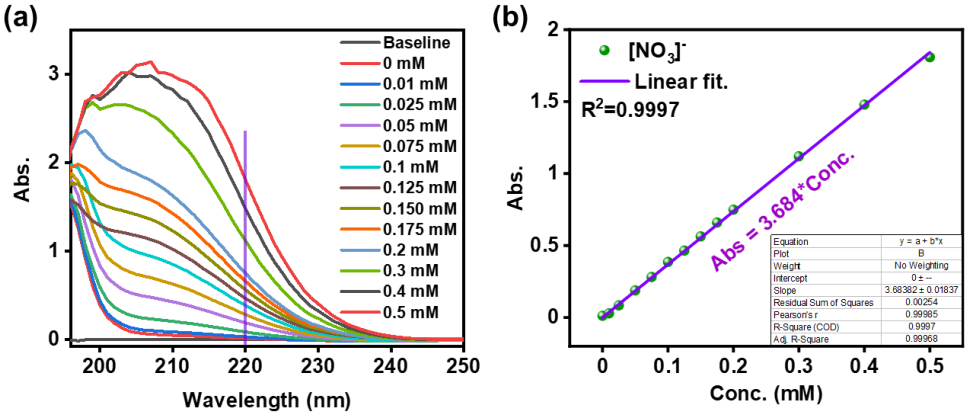

Figure S28. Calibration curves made with different concentrations of nitrate. (a) Electronic spectra of concentrations from 0 mM to 0.5 mM of KNO_3, and (b) absorbance vs. concentration plot at the wavelength of 220 nm represent the calibration curve for $[NO_3]^-$.[27]

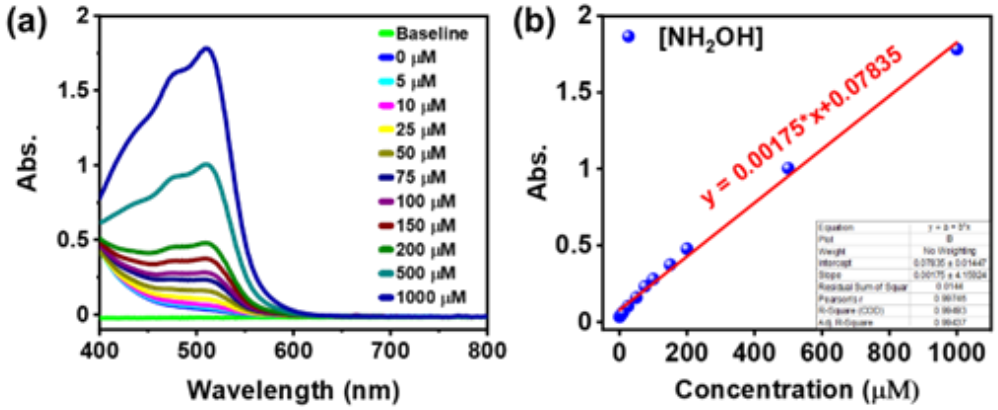

Figure 29. Calibration curves made with different concentrations of hydroxyl amine (NH_2OH). (a) Electronic spectra of concentrations from 0 µM to 1000 µM of NH_2OH, and (b) absorbance vs. concentration plot at the wavelength of 510 nm represent the calibration curve for NH_2OH.[28]

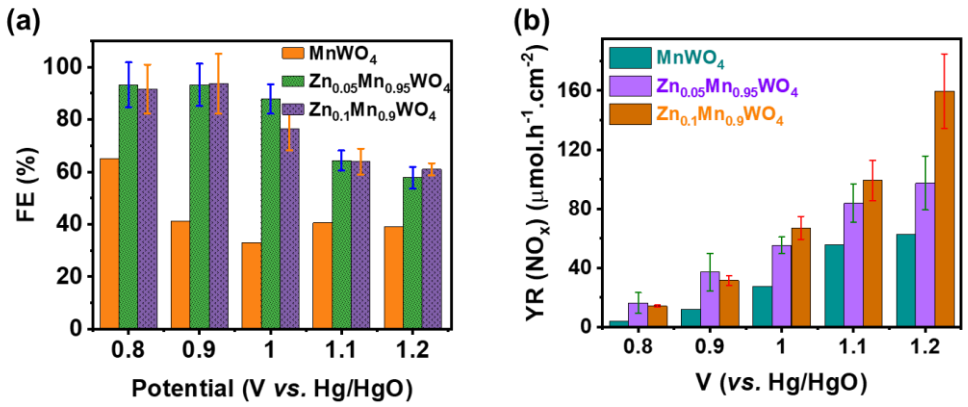

Figure S30. Comparison of total (a) Faradaic efficiency, and (b) yield rate of $[NO_{2/3}]^-$ formed during AOR catalysed by $Zn_xMn_{1-x}WO_4$ and undoped $MnWO_4$.

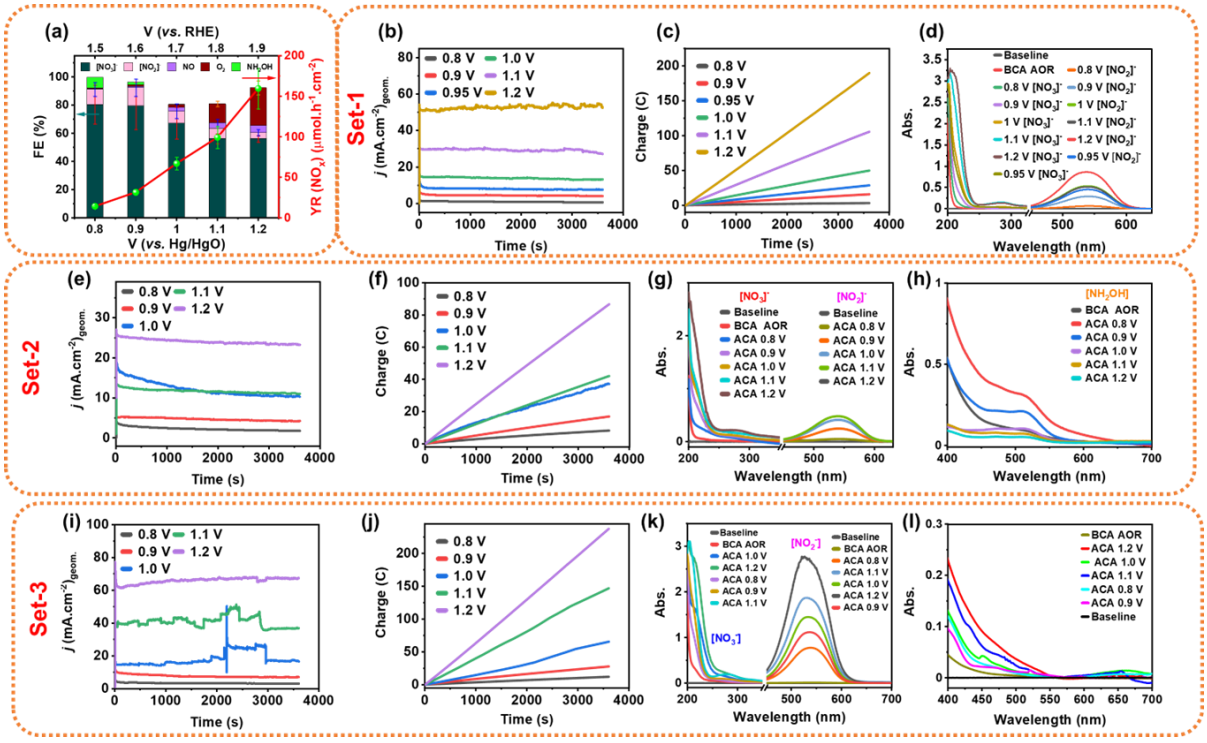

Figure S31. Spectrophotometric quantification of $[NO_{2/3}]^-$ product formed via AOR using $Zn_{0.1}Mn_{0.9}WO_4$/NF as working electrode, 0.5 M NH_3 in 0.5 M Na_2SO_4 as electrolyte, and at different applied potentials. (a) FE and cumulative yield rate of $[NO_{2/3}]^-$ for AOR at different potentials. Time vs. current plot during CA-AOR of (b) Set 1, (e) Set 2, (i) Set 3; and corresponding time vs. charge plots (c) Set 1, (f) Set 2, (j) Set 3. UV-vis absorption spectra obtained after 1 h bulk electrolysis at various potentials for nitrate ($[NO_3]^-$) (range from 200 to 350 nm), and nitrite ($[NO_2]^-$) (range from 450 to 650 nm) of (d) Set 1, (g) Set 2, (k) Set 3. UV-vis absorption spectra obtained after 1 h bulk electrolysis at various potentials for hydroxyl amine ($[NH_2OH]$) of (h) Set 2, (l) Set 3. (BCA= Before chronoamperometric study; ACA= After chronoamperometric study)

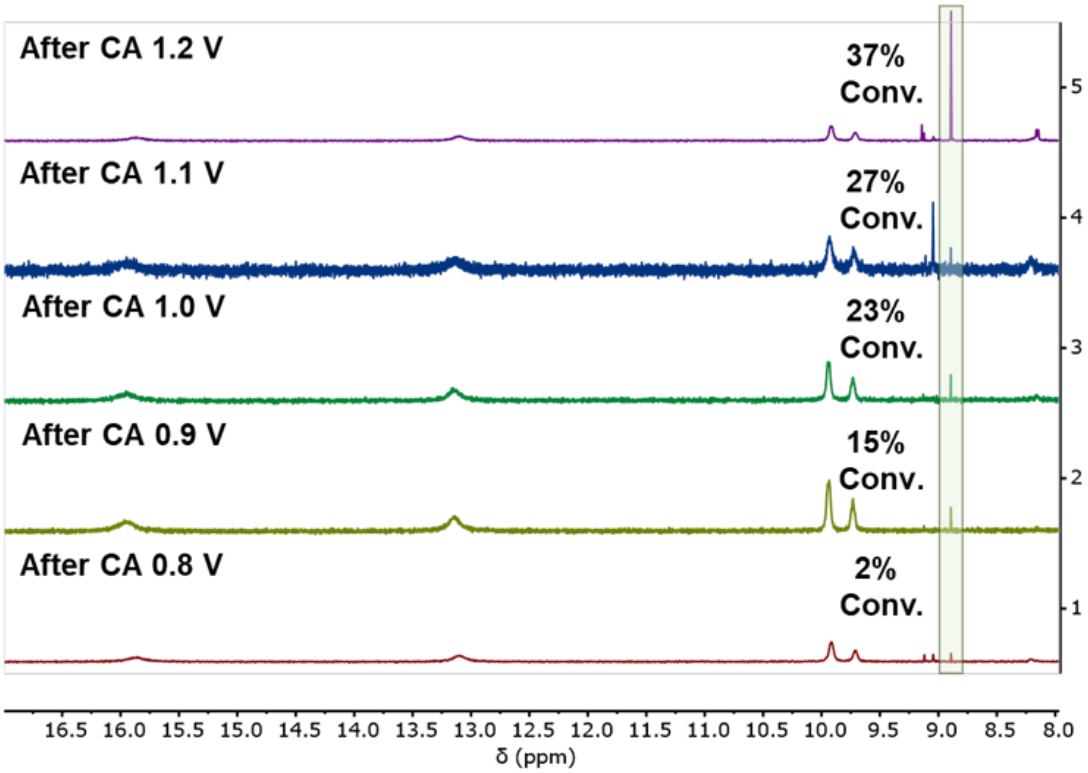

Figure S32. ^{1}H-NMR spectra of 1 mM cobalt tetraphenyl porphyrin (Co-TPP) complex after reacting with NO generated from AOR using $Zn_{0.1}Mn_{0.9}WO_4$/NF as anode, 0.5 M NH_3 in 0.5 M Na_2SO_4 as electrolyte, and under different applied potentials. The quantity (moles) of NO formed during AOR was calculated from the area (intensity) of the ^{1}H peak at 8.9 ppm, which originated due to binding of NO with the Co-TPP complex.[29]

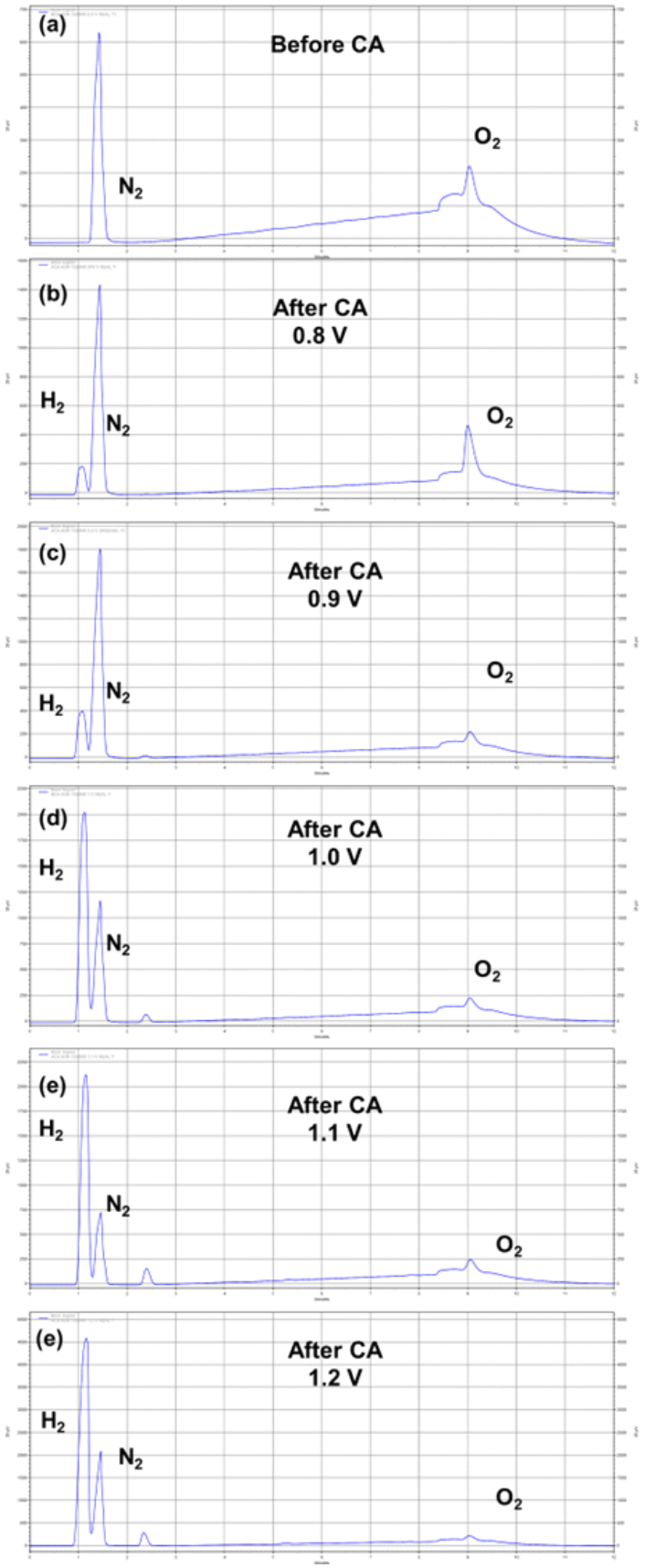

Figure S33. Chromatograms of the gaseous products formed during AOR performed in single compartment cell; (a) before CA, and after CA at (b) 0.8 V, (c) 0.9 V, (d) 1.0 V, (e) 1.1 V, and (e) 1.2 V for 1 hour using $Zn_{0.1}Mn_{0.9}WO_4$/NF anode.

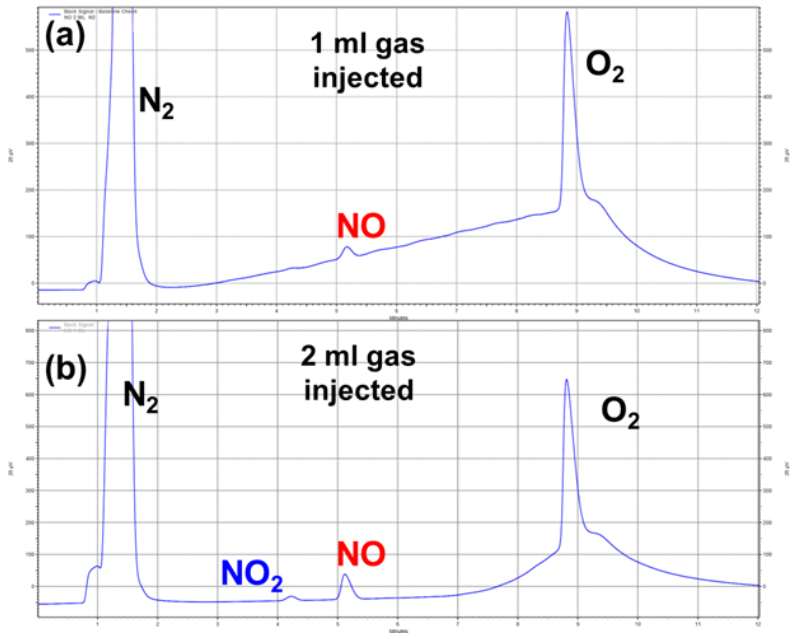

Figure S34. Chromatograms obtained from the different volumes of nitrous oxide (NO)-containing (retention time for NO: 5.1) gas mixture of (a) 1 mL and (b) 2 mL.

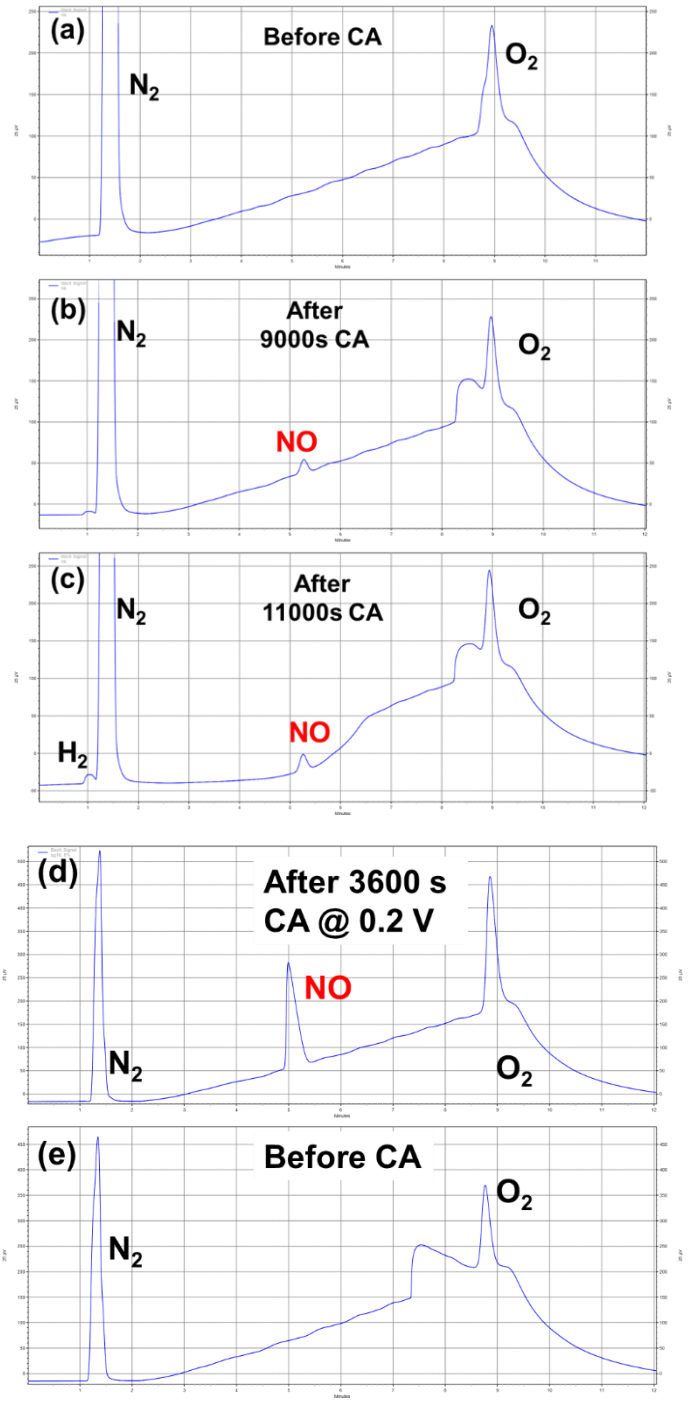

Figure S35. Chromatograms of the gaseous products (NO) formed during AOR (a) before AOR, after (b) 9000 s, and (c) 11000 s of CA performed in Hoffman apparatus (inverted burette cell set-up, see Figure S59) using $Zn_{0.1}Mn_{0.9}WO_4$/NF anode. (d) After CA for 1 h at an applied potential of 0.2 V (vs. Hg/HgO) in presence of hydroxyl amine in the electrolyte instead of ammoina, (e) before CA in presence of hydroxyl amine.

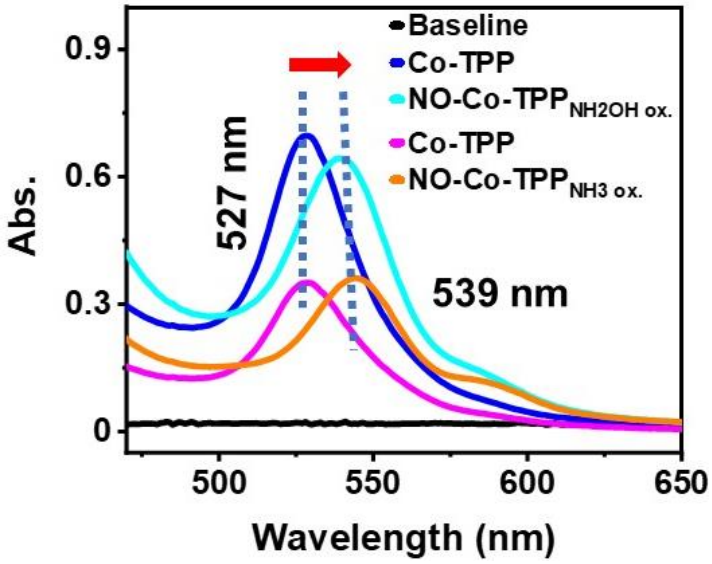

Figure S36. Optical spectra of blank cobalt tetraphenyl porphyrin (Co-TPP) complex and after reacting with NO generated from the hydroxyl amine (NH_2OH) oxidation at applied potential of 0.2 V (vs. Hg/HgO) for 1 h (before oxidation blue and after oxidation cyan colour) and ammonia (NH_3) oxidation reaction (AOR) (before oxidation pink and after oxidation orange colour) 0.9 V (vs. Hg/HgO) for 1 h.

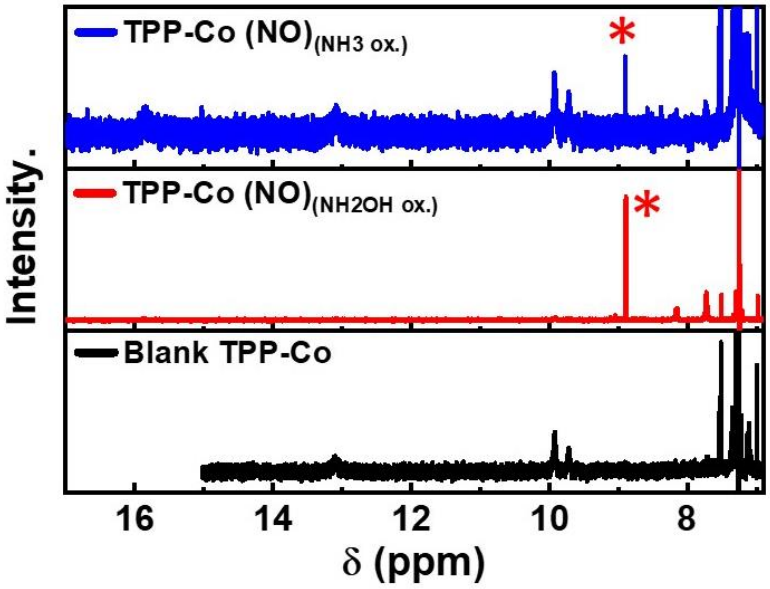

Figure S37. ^{1}H-NMR spectra of blank cobalt tetraphenyl porphyrin (Co-TPP) complex (black) and NO-bound complex formed from the gas generated by hydroxyl amine oxidation (red) and AOR (blue).[29]

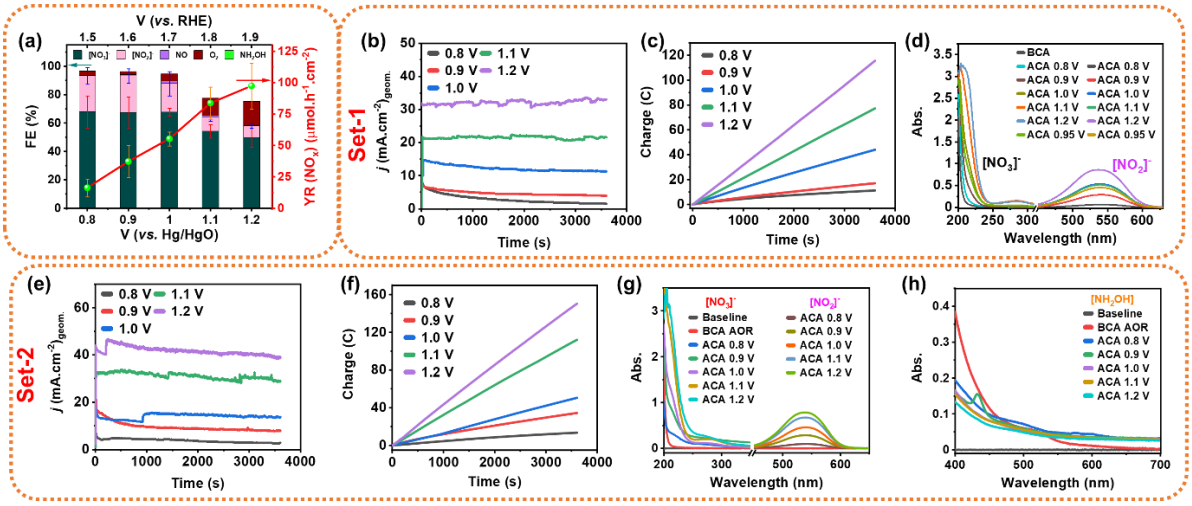

Figure S38. AOR study conducted at different applied potentials in 0.5 M Na_2SO_4 containing 0.5 M NH_3 using $Zn_{0.05}Mn_{0.95}WO_4$/NF as anode and quantification of $[NO_{2/3}]^-$ product via electronic spectroscopy. (a) FE and cumulative yield rate of $[NO_{2/3}]^-$ for AOR at different potentials. (b, e) Time vs. current and (c, f) corresponding time vs. charge plots during the bulk electrolysis study at five different potentials of set 1 and 2, respectively. (d, g) UV-vis absorption spectra obtained after 1 h bulk electrolysis at various potentials for nitrate ($[NO_3]^-$) (range from 200 to 350 nm), nitrite ($[NO_2]^-$) (range from 450 to 650 nm) of set 1 and 2, respectively. UV-vis absorption spectra obtained after 1 h bulk electrolysis at various potentials for hydroxyl amine ($[NH_2OH]$) of (h) Set 2. (BCA= Before chronoamperometry test; ACA= After chronoamperometry test)

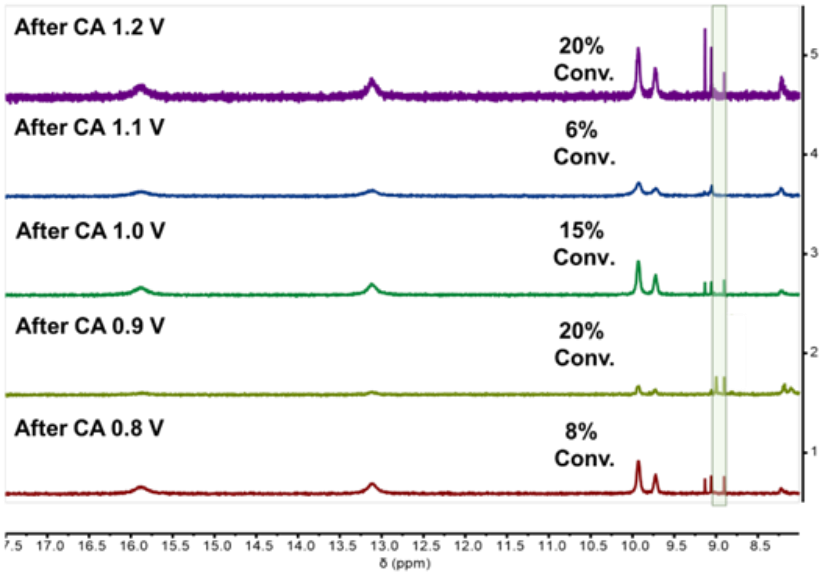

Figure S39. ^{1}H-NMR spectra of 1 mM cobalt tetraphenyl porphyrin (Co-TPP) complex after reacting with NO generated from CA-AOR performed with $Zn_{0.05}Mn_{0.95}WO_4$/NF anode in 0.5 M Na_2SO_4 containing 0.5 M NH_3 at different applied potentials. The quantity (moles) of NO formed during AOR was calculated from the area (intensity) of the ^{1}H peak at 8.9 ppm, which originated due to binding of NO with the Co-TPP complex.[29]

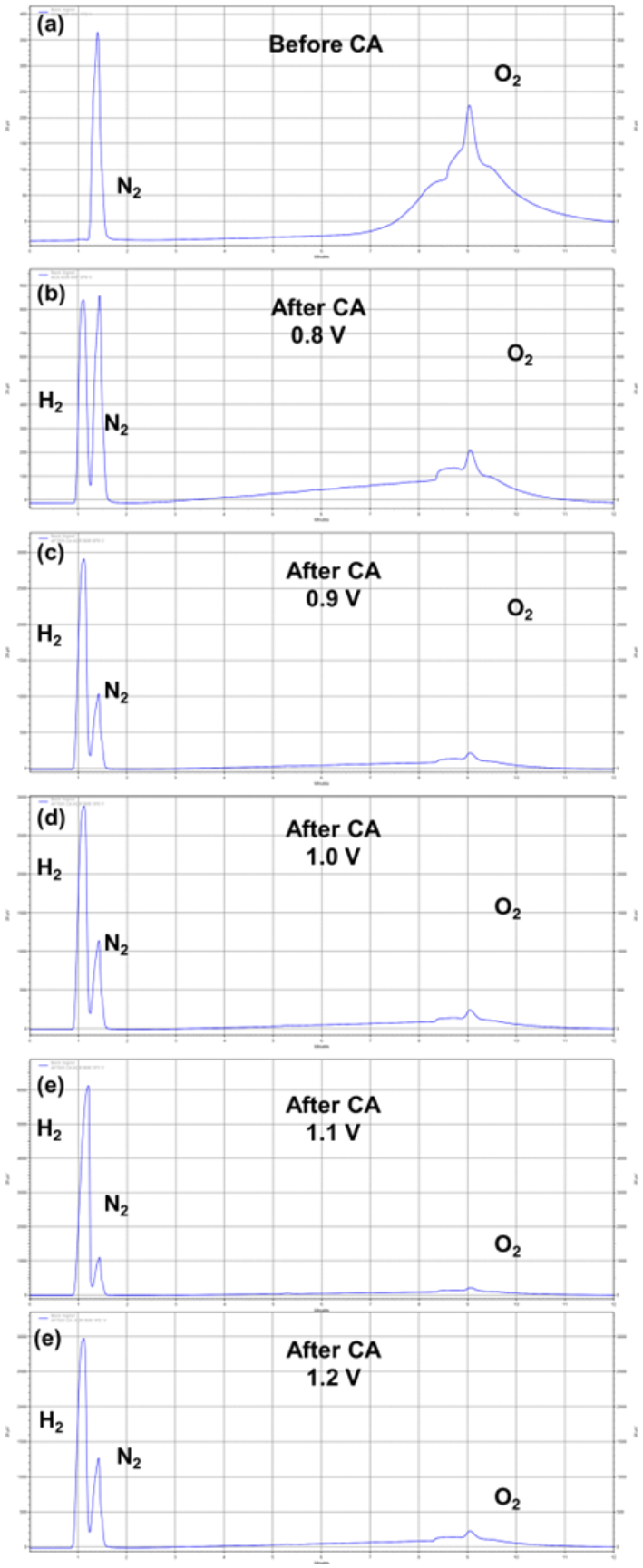

Figure S40. Chromatograms of the gaseous products formed during AOR performed in single compartment cell; (a) before CA, and after CA at (b) 0.8 V, (c) 0.9 V, (d) 1.0 V, (e) 1.1 V, and (e) 1.2 V for 1 hour using $Zn_{0.05}Mn_{0.95}WO_4$/NF anode.

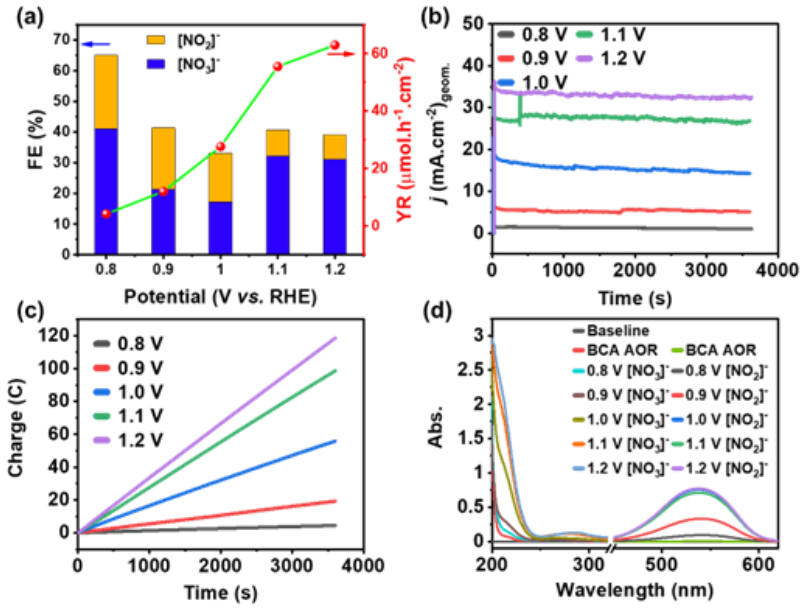

Figure S41. AOR in 0.5 M NH_3 containing 0.5 M Na_2SO_4 with $MnWO_4$/NF at different applied potential and quantification of $[NO_{2/3}]^-$ product. (a) Faradaic efficiency and cumulative yield rate of $[NO_{2/3}]^-$ for AOR at different potentials. (b)Time vs. current and (c) corresponding time vs. charge plot during bulk electrolysis stydy at six different potential. (d) UV-vis absorption spectra obtained after 1 h bulk electrolysis at various potentials for nitrate ($[NO_3]^-$) (range from 200 to 350 nm), nitrite ($[NO_2]^-$) (range from 450 to 650 nm).

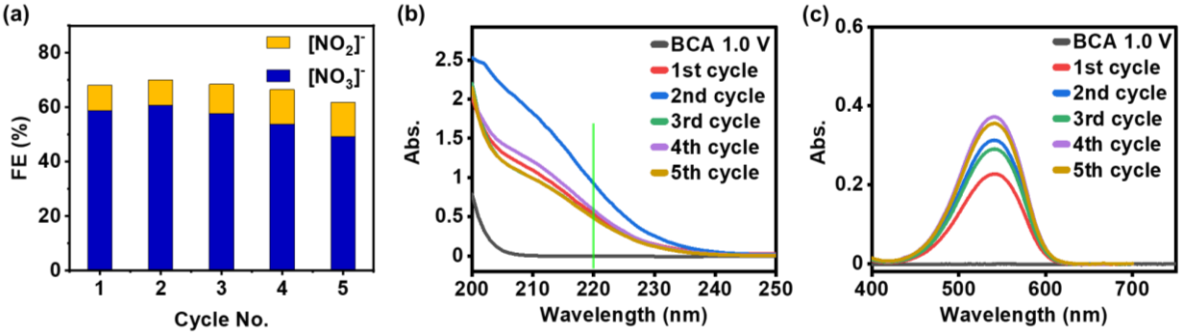

Figure S42. Reproducability test for $Zn_{0.1}Mn_{0.9}WO_4$/NF up to 5 cycles of AOR-CA, showing 70±5 % $[NO_{2/3}]^-$ selectivity at 1.0 V (vs. Hg/HgO) applied potential for 3600 s. (a) FE with the number of cycles. UV-vis absorption spectra for (b) nitrate, (c) nitrite. (In the 2nd cycle, due to the increased time of 5200 s, nitrate production is higher than that of the others).

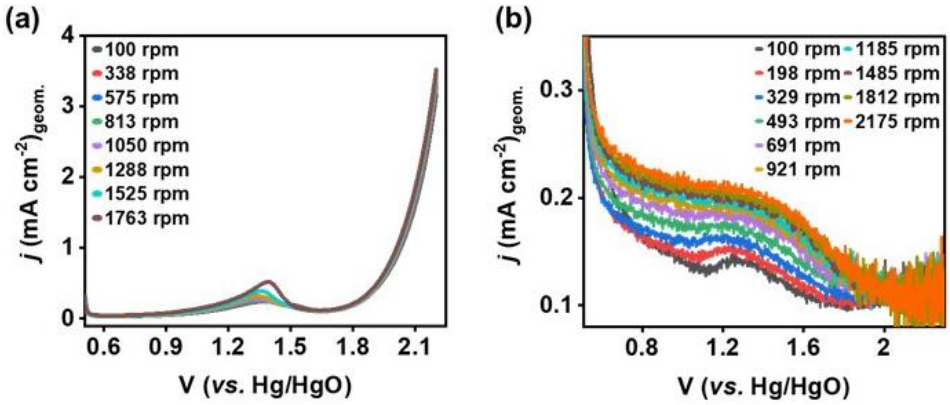

Figure S43. (a) Disk current for RRDE study in 0.5 M Na_2SO_4, and (b) ring current for RRDE study in 0.5 M Na_2SO_4 containing 25 mM NH_3 using $Zn_{0.1}Mn_{0.9}WO_4$/GC working electrode.

Table S5. RRDE data analysis based on the K-L analysis at different applied potentials.

Potential (V)	K- L Analysis		No. of electron transferred	No. of e^- change (av.)	k_{obs} ($\times10^{-3}$)	k_{obs} (av.) ($\times10^{-3}$)
	Slope	Intercept				
2.05	1643.5	54.74	1.864	**2.12 (±0.2)**	20.71830785	**4.915 (±3)**
1.95	1665.0	82.023	1.84		14.00720583	
1.9	1621.4	115.63	1.89		9.673255371	
1.85	1585.4	163.89	1.9331		6.672647872	
1.8	1540.1	163.89	1.9899		6.482182824	
1.75	1426.0	297.73	2.149		3.304045125	
1.7	1262.6	419.36	2.427		2.077055987	
1.65	1071.6	576.05	2.86		1.283153961	

*Red-marked values correspond to data in the limiting current range, which was not taken into account to determine the k_{obs}, which solely comes from charge transfer limiting current and negligible contribution from kinetic current.

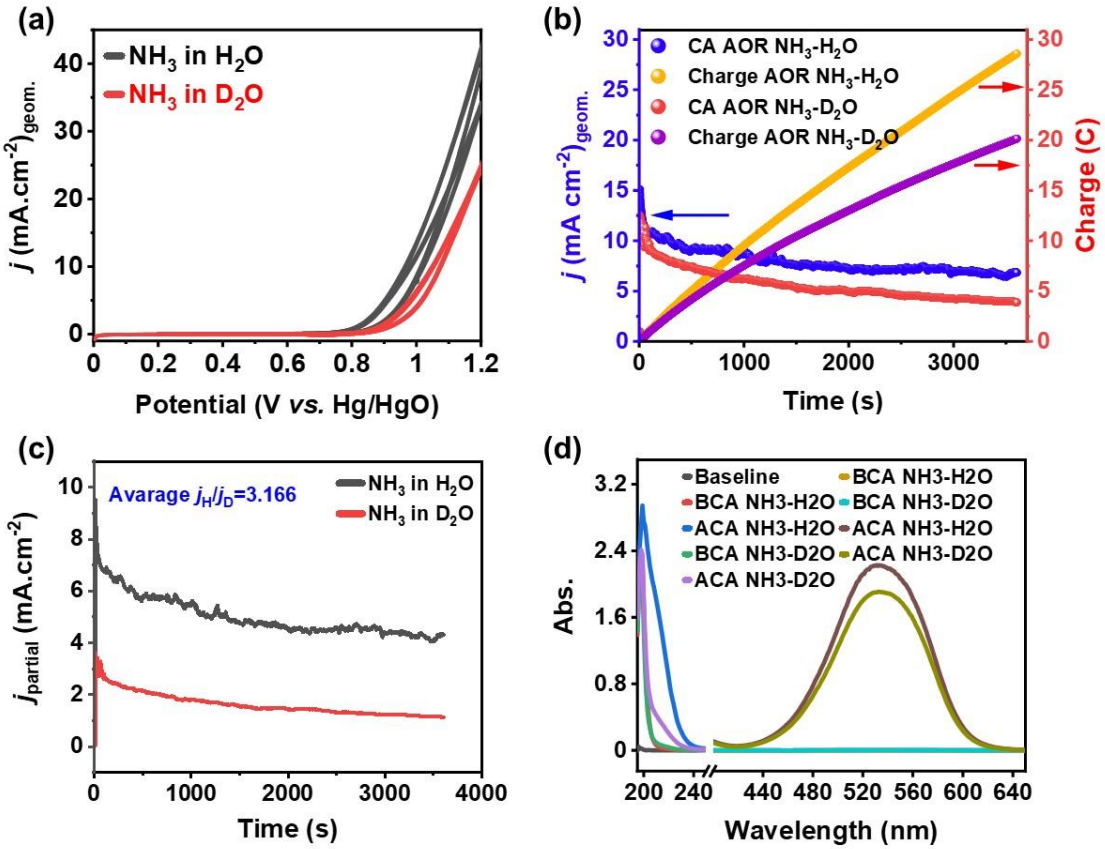

Figure S44. (a) Cyclic voltammetry (CV) studies for AOR with $Zn_{0.1}Mn_{0.9}WO_4$/NF performed in NH_3 containng D_2O and H_2O. (b) Current and charge vs time plots for the bCA study in H_2O and D_2O. (c) Partial current density for $[NO_{2/3}]^-$ production with a KIE value obtained of 3.2. (d) Quantification of $[NO_{2/3}]^-$ in D_2O through optical spectroscopy (UV-vis), (200 to 250 nm for nitrate and 400 to 650 nm range for nitrite, BCA= Before chronoamperometry test; ACA= After chronoamperometry test).

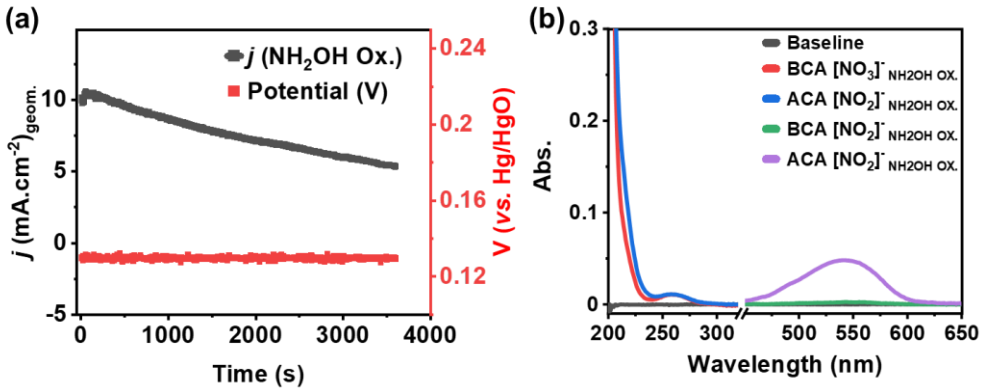

Figure S45. (a) Time vs. current plot of bulk electrolysis study (red) and amount of charge delivered during electrocatalysis (black) observed during hydroxyl amine oxidation using $Zn_{0.1}Mn_{0.9}WO_4$/NF at 0.35 V (vs. Hg/HgO). (b) UV-vis absorption spectra obtained after 1 h bulk electrolysis for nitrate ($[NO_3]^-$) (range from 200 to 350 nm), nitrite ($[NO_2]^-$) (range from 450 to 650 nm). (BCA= Before chronoamperometry test; ACA= After chronoamperometry test)

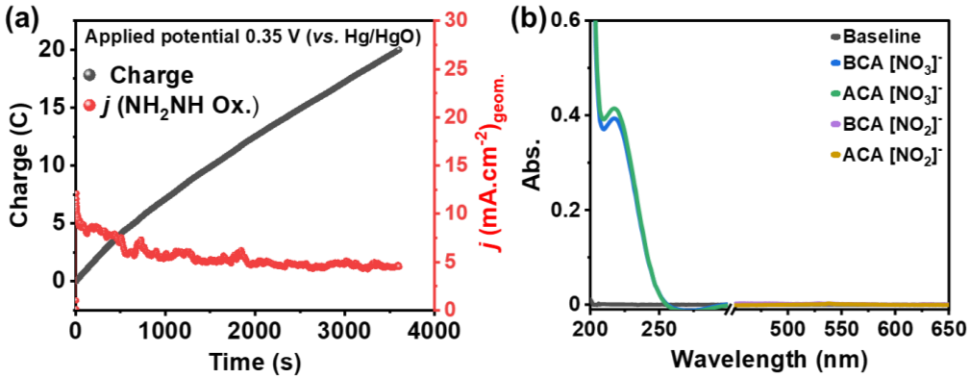

Figure S46. (a) Current vs. time plot of bulk electrolysis study (black) and applied constant potential (red) for the hydrazine oxidation using $Zn_{0.1}Mn_{0.9}WO_4$/NF at 0.14 V (vs. Hg/HgO) applied potentials in 0.5 M NH_2NH_2 containing 0.5 M Na_2SO_4. (b) UV-vis absorption spectra obtained after 1 h bulk electrolysis for nitrate ($[NO_3]^-$) (range from 200 to 350 nm), nitrite ($[NO_2]^-$) (range from 450 to 650 nm). (BCA= Before chronoamperometry test; ACA= After chronoamperometry test)

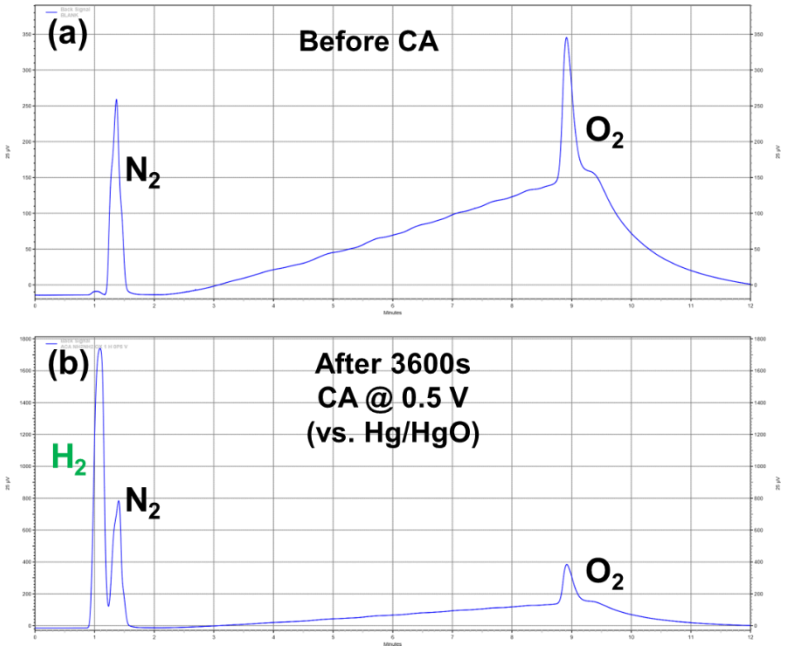

Figure S47. Gas chromatograms of the gaseous products during hydrazine oxidation at (a) before bulk electrolysis (CA test) and after (b) 3600 s using $Zn_{0.1}Mn_{0.9}WO_4$/NF anode.

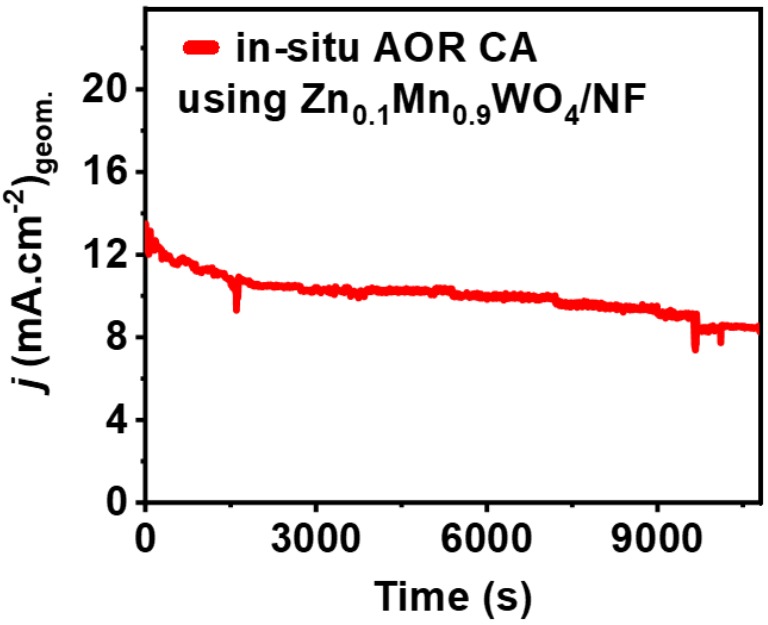

Figure S48. J vs t plot of CA study performed at an applied potential of 0.9 V (vs. Hg/HgO) for 3 h for the in-situ IR study.

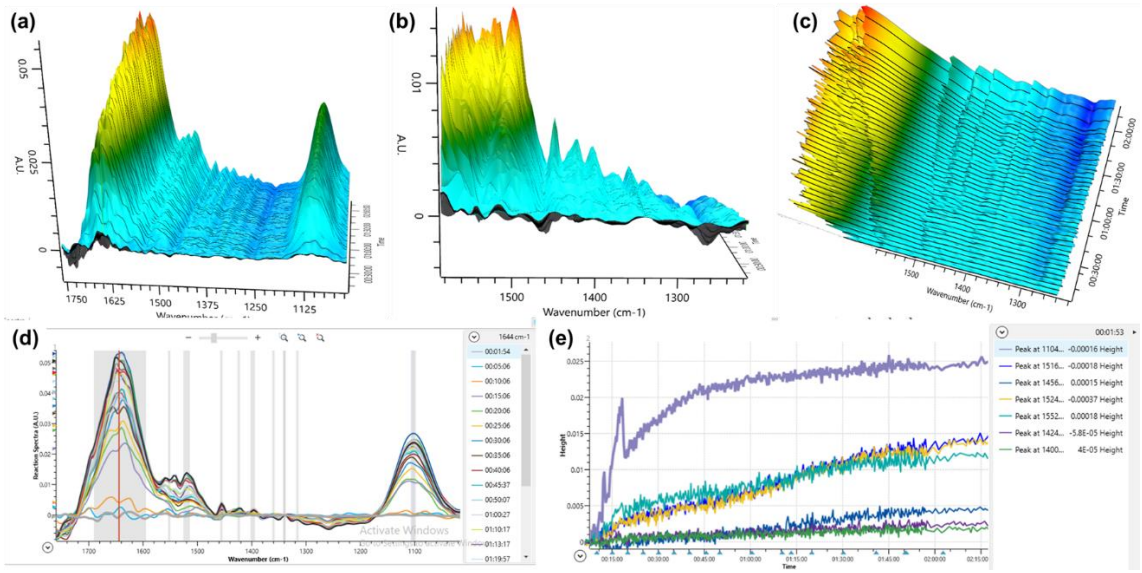

Figure S49. In-situ IR spectra acquired during AOR catalysed by $Zn_{0.1}Mn_{0.9}WO_4$/NF for 2 h at an applied potential of 0.8 V (vs. Hg/HgO) in 0.5 M Na_2SO_4 containing 0.5 M NH_3 at room temperature (28 ºC). (a-c) Zoomed Surface spectrum or 3-D spectra of in-situ IR spectra at wavenumber of 1000-1800 cm^{-1}. (d) Some selected 2D spectra recorded during AOR. (e) Concentration trends with time of some selected key peak intensities increased during AOR.[12]

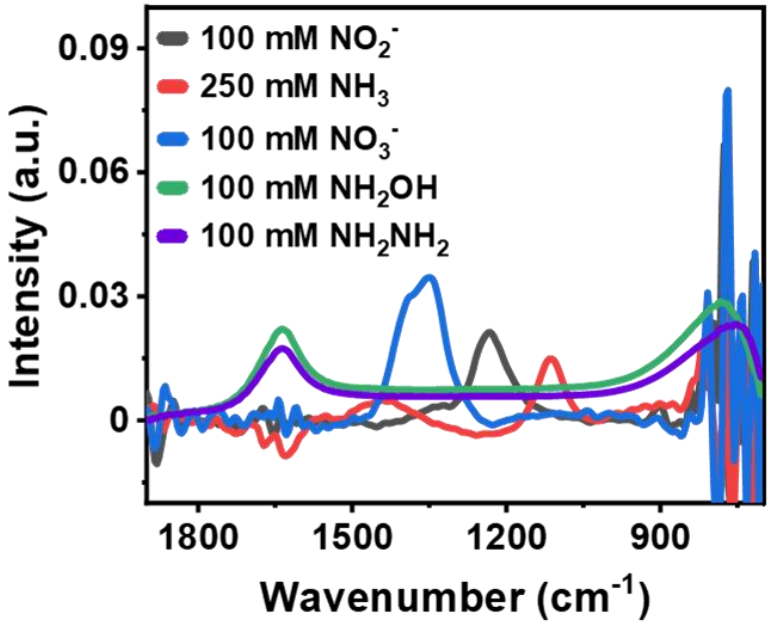

Figure S50. Characteristic (solution) IR spectra of standard sample solutions made in deionised water.

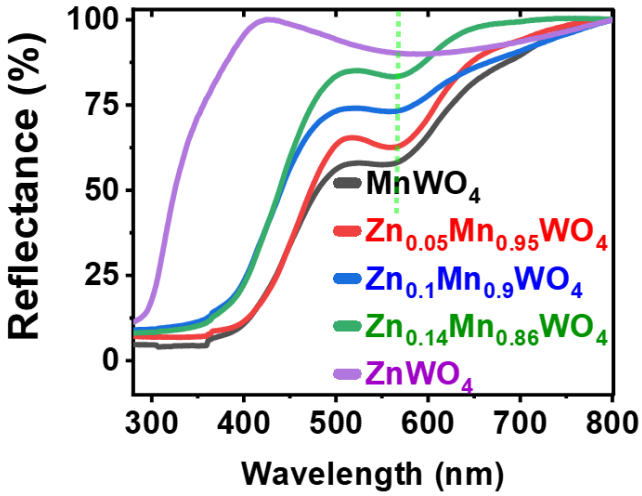

Figure S51. UV-VIS diffuse reflectance spectra (DRS) of $MnWO_4$, $ZnWO_4$, and different percentages of Zn-doped $MnWO_4$.

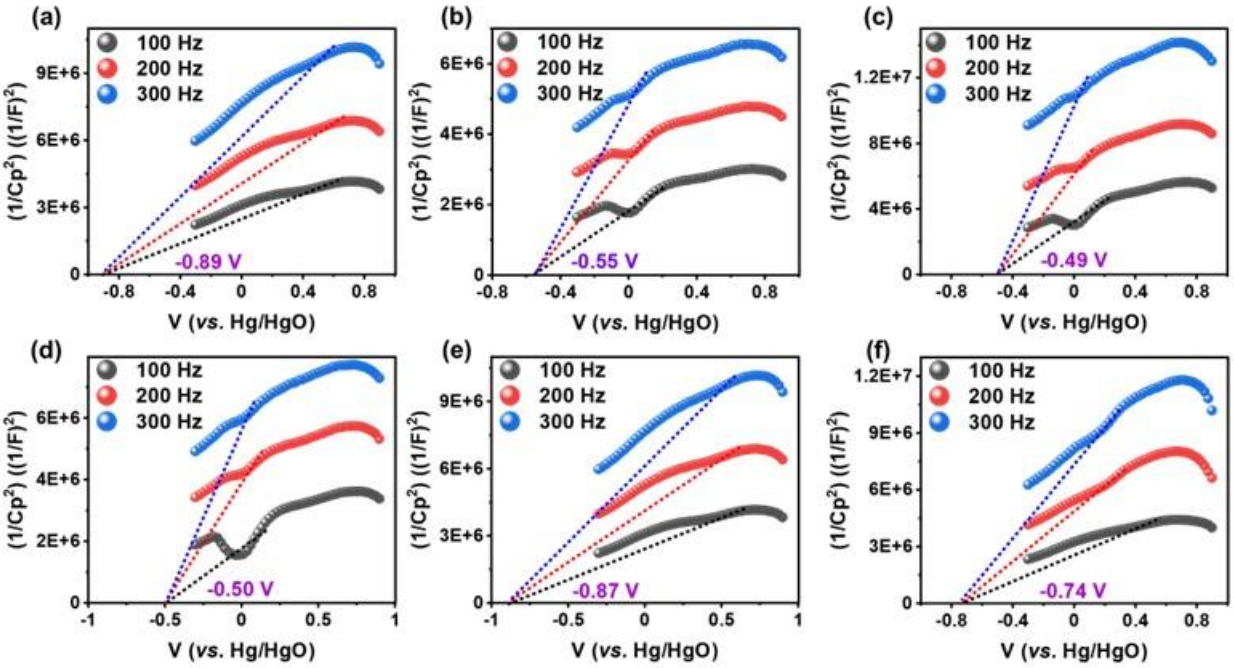

Figure S52. Mott-Schottky plot of material in 0.5 M Na_2SO_4 containing 0.5 M NH_3 at an applied potential range of -1 to 1 V (vs. Hg/HgO) using (a) $MnWO_4$, (b) $Zn_{0.05}Mn_{0.95}WO_4$, (c) $Zn_{0.1}Mn_{0.9}WO_4$, (d) $Zn_{0.14}Mn_{0.86}WO_4$, (e) $ZnWO_4$, and (f) bare carbon paper (CP) electrode.

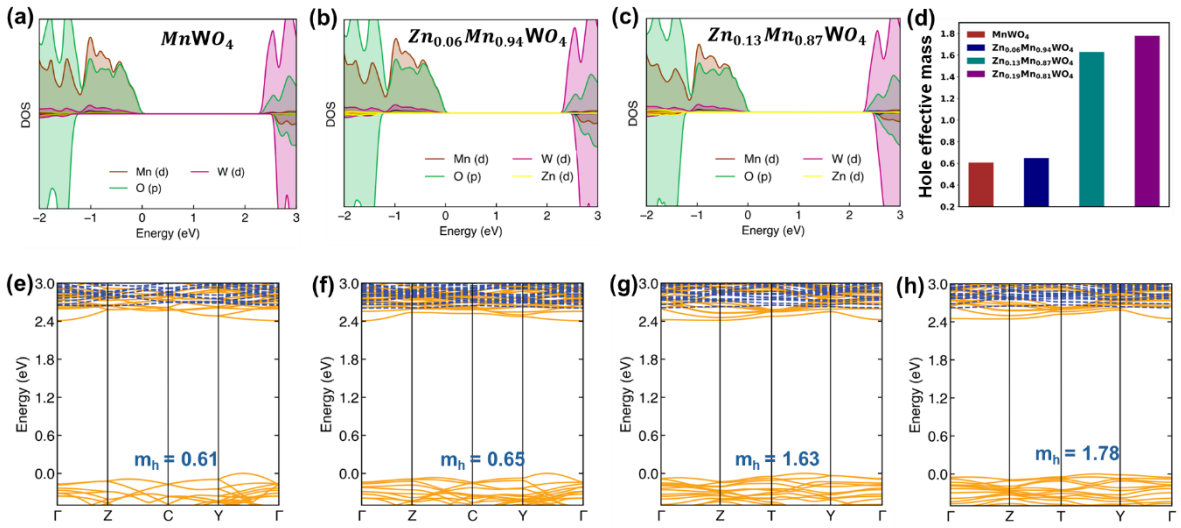

Figure S53. Projected density of states (pDOS) for (a) $MnWO_4$ (b) $Zn_{0.06}Mn_{0.94}WO_4$ (c) $Zn_{0.13}Mn_{0.87}WO_4$ calculated by using the density functional theory (DFT) + U-based simulations. (d) Hole effective mass comparison between pristine $MnWO_4$ and Zn-doped compositions ($Zn_{0.06}Mn_{0.94}WO_4$, $Zn_{0.13}Mn_{0.87}WO_4$ and $Zn_{0.19}Mn_{0.81}WO_4$). Band structure of (a) $MnWO_4$ (b) $Zn_{0.06}Mn_{0.94}WO_4$ (c) $Zn_{0.13}Mn_{0.87}WO_4$ and (d) $Zn_{0.19}Mn_{0.81}WO_4$.

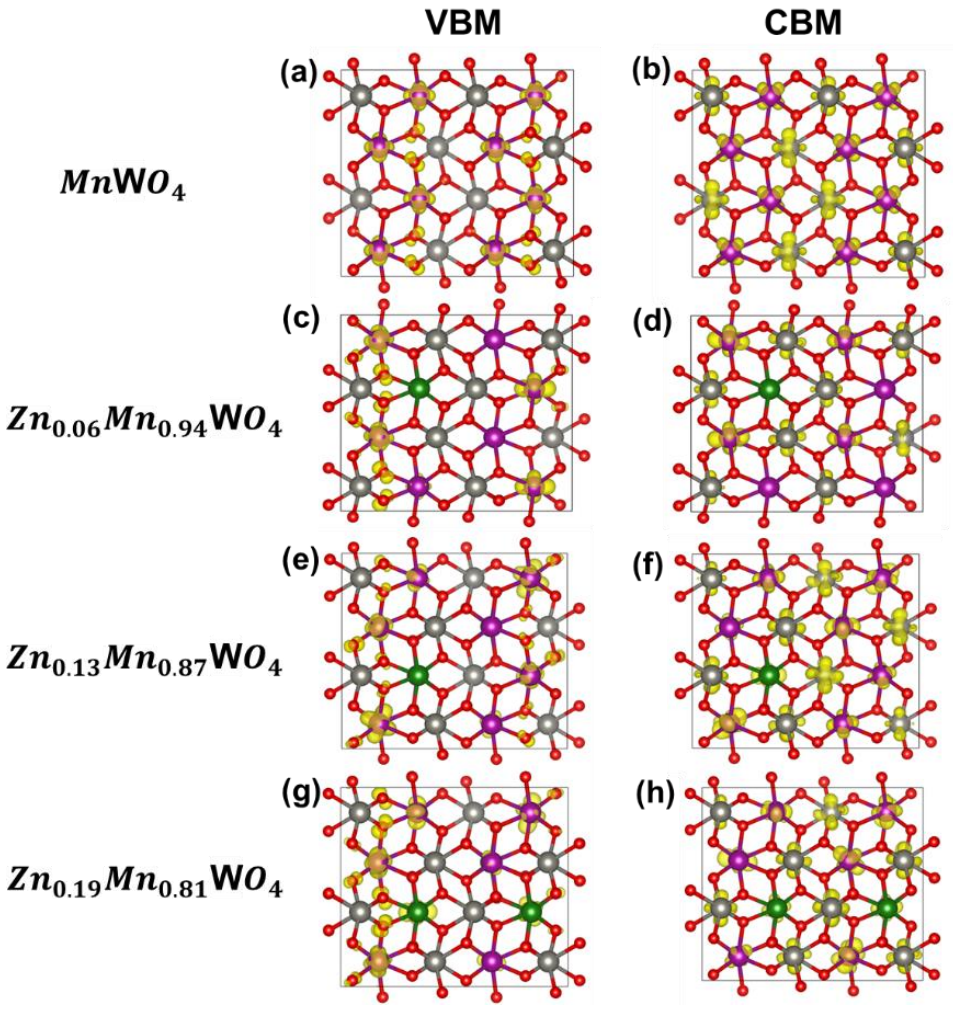

Figure S54. Band-decomposed charge density distributions for VBM and CBM states plotted at an iso-surface value of 3.24×10^{-5} e/Å^3. (a,b) Pristine MnWO4 showing homogeneous VBM charge density on Mn (purple) and O (red) atoms, and CBM on W (grey), Mn (purple) atoms. (c-h) Zn-doped compositions with increasing Zn concentration (green atoms) demonstrating progressive charge localization in VBM states around specific Mn-O units, while CBM remains distributed. Zn atoms show no electron density contribution, confirming their electronically inert nature. The yellow-colored regions represent spatial distributions where electron density exceeds the isosurface value of 3.24×10^{-5} e/Å^3.

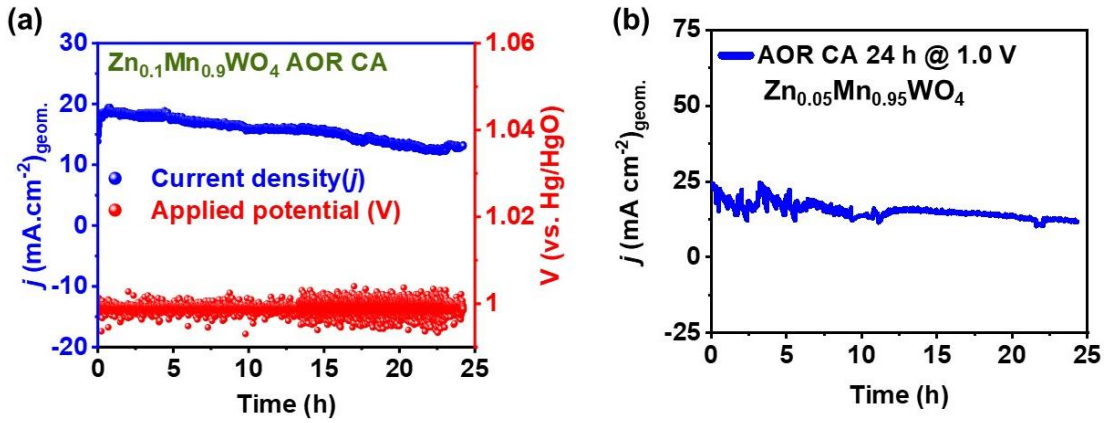

Figure S55. CA study using (a) $Zn_{0.1}Mn_{0.9}WO_4$/NF and (b) $Zn_{0.05}Mn_{0.95}WO_4$/NF in 0.5 M Na_2SO_4 containing 0.5 M NH_3 for 24 hours at an applied potential of 1.0 V (vs. Hg/HgO).

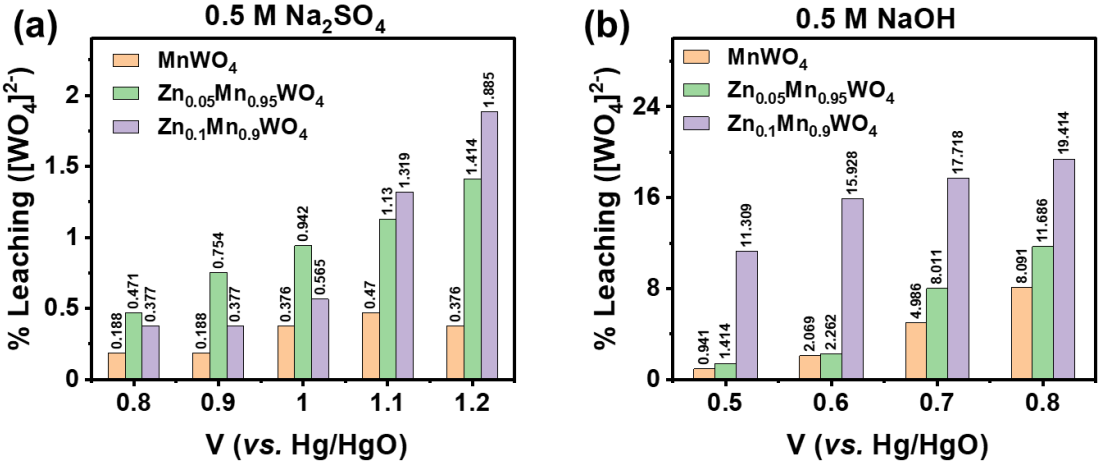

Figure S56. ICP-OES study of the electrolytes, (a) 0.5 M Na_2SO_4 containing 0.5 M NH_3, and (b) 0.5 M NaOH containing 0.5 M NH_3 and plot of $[WO_4]^{2-}$ leaching percentage from different anodes (mentioned in the inset) after CA-AOR for 1 h at different potentials.

Table S6. ICP-OES data for the electrolytes obtained after the CA-AOR performed at different potentials with $MnWO_4$ and $Zn_xMn_{1-x}WO_4$ in 0.5 M NH_3 containing 0.5 Na_2SO_4.

Samples	Condition (Na_2SO_4)	Applied potential (V)	Leaching amount (ppm)	% W leaching
$MnWO_4$	Na_2SO_4	0.8	0.02	0.188
		0.9	0.02	0.188
		1.0	0.04	0.376
		1.1	0.05	0.470
		1.2	0.04	0.376

$Zn_{0.05}Mn_{0.95}WO_4$	Na_2SO_4	0.8	0.05	0.471
		0.9	0.08	0.754
		1.0	0.10	0.942
		1.1	0.12	1.130
		1.2	0.15	1.414
		1.0[#]	**1.02**	**9.87**
$Zn_{0.1}Mn_{0.9}WO_4$	Na_2SO_4	0.8	0.04	0.377
		0.9	0.04	0.377
		1.0	0.06	0.565
		1.1	0.14	1.319
		1.2	0.20	1.885
		1.0[#]	**1.11**	**10.367**

[#]after 24 h of CA-AOR

Table S7. ICP-OES data for the electrolytes of the CA performed at different potentials with $MnWO_4$ and $Zn_xMn_{1-x}WO_4$ in 0.5 M NH_3 containing 0.5 M NaOH.

Samples	**Condition**	**Applied Potential (V)**	**Leaching Amount (ppm)**	**% W Leaching**
$MnWO_4$	NaOH	0.5	0.10	0.941
		0.6	0.22	2.069
		0.7	0.53	4.986
		0.8	0.86	8.091
		0.9	1.02	9.596
$Zn_{0.05}Mn_{0.95}WO_4$	NaOH	0.5	0.15	1.414
		0.6	0.24	2.262
		0.7	0.85	8.011
		0.8	1.24	11.686
		0.9	0.97	9.142
$Zn_{0.1}Mn_{0.9}WO_4$	NaOH	0.5	1.20	11.309
		0.6	1.69	15.928
		0.7	1.88	17.718
		0.8	2.06	19.414

		0.9	2.18	20.545

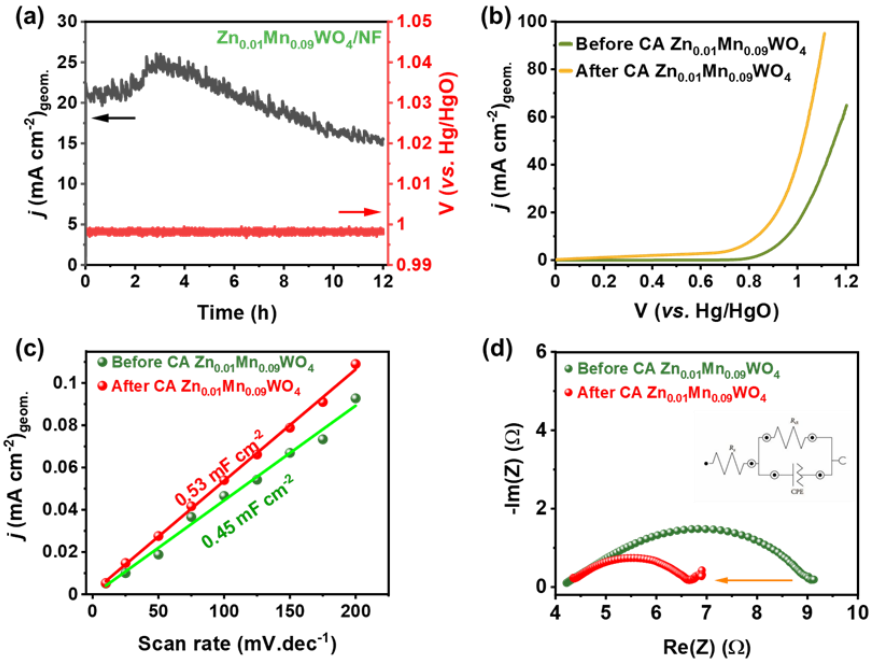

Figure S57. (a) CA-AOR using $Zn_{0.1}Mn_{0.9}WO_4$/NF electrode at 1.0 V (vs. Hg/HgO) for 12 h. (b) LSV polarization curves, (c) C_{dl}, and (d) EIS at 1.0 V vs. Hg/HgO, before and after 12 h CA.

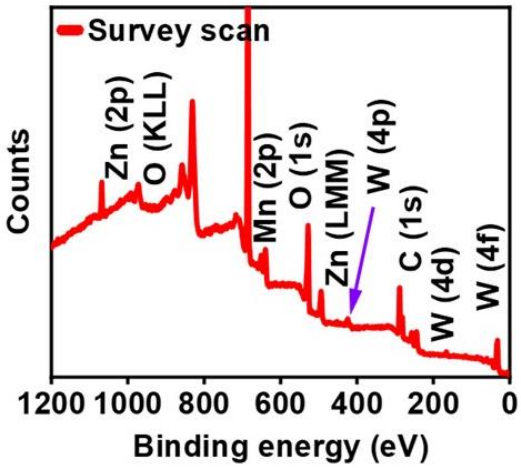

Figure S58. XPS survey spectrum recorded with the sample isolated from the $Zn_{0.1}Mn_{0.9}WO_4$/NF electrode after 24 h CA at 1.0 V (vs. Hg/HgO).

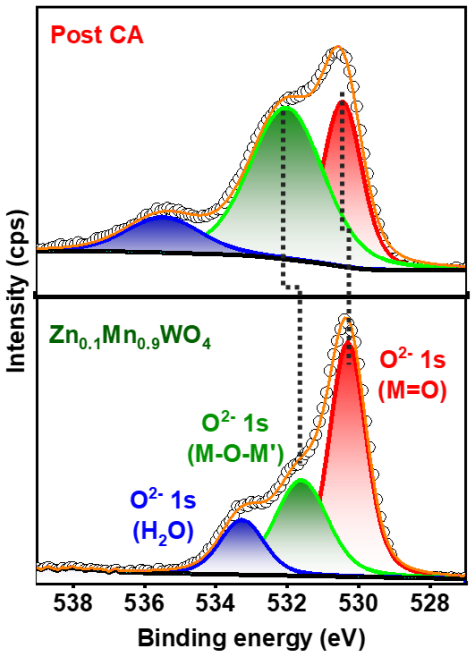

Figure S59. Comparison of the deconvoluted core-level O 1s XPS spectra before and after 24 h CA-AOR study.

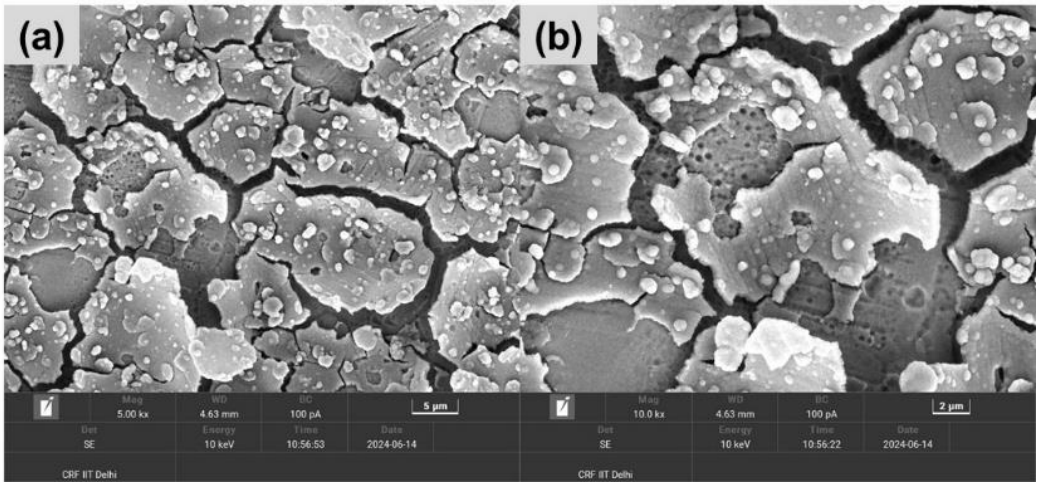

Figure S60. Post-catalytic FE-SEM image of the used $Zn_{0.1}Mn_{0.9}WO_4$/NF electrode after 24 h CA at an applied potential of 1.0 V (vs. Hg/HgO).

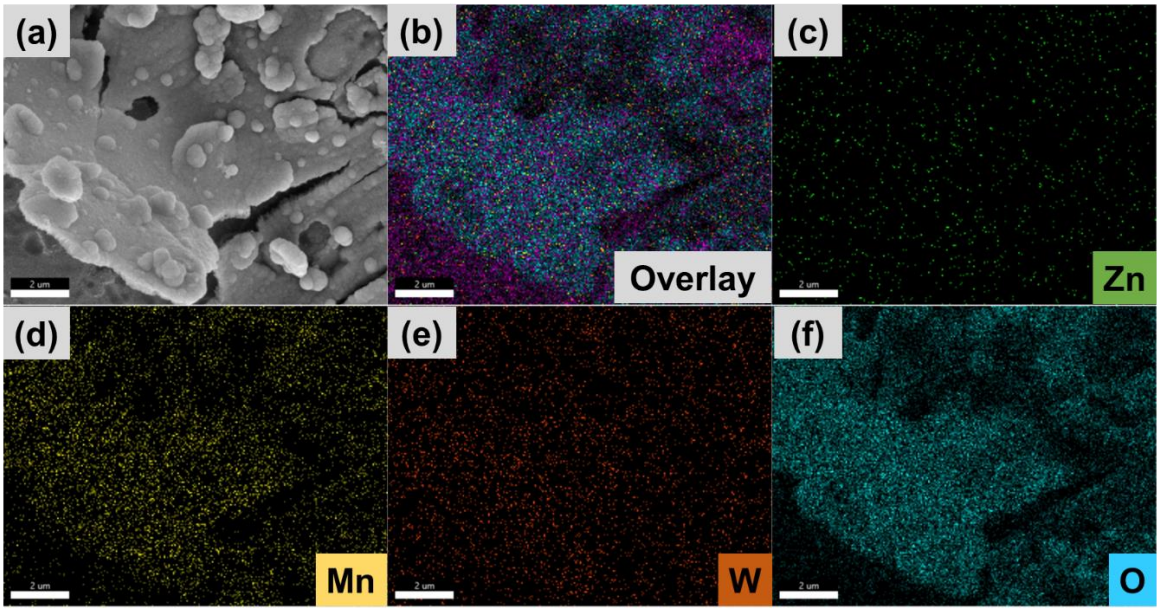

Figure S61. (a) FE-SEM image of the used $Zn_{0.1}Mn_{0.9}WO_4$/NF electrode after 24 h CA at 1.0 V (vs. Hg/HgO), (b) overlay of all elements, elemental mapping for (c) Zn, (d) Mn, (e) W, and (f) O (in the overlay, pink colour represent Ni from the Ni-foam electrode support; scale bar: 2 µm).

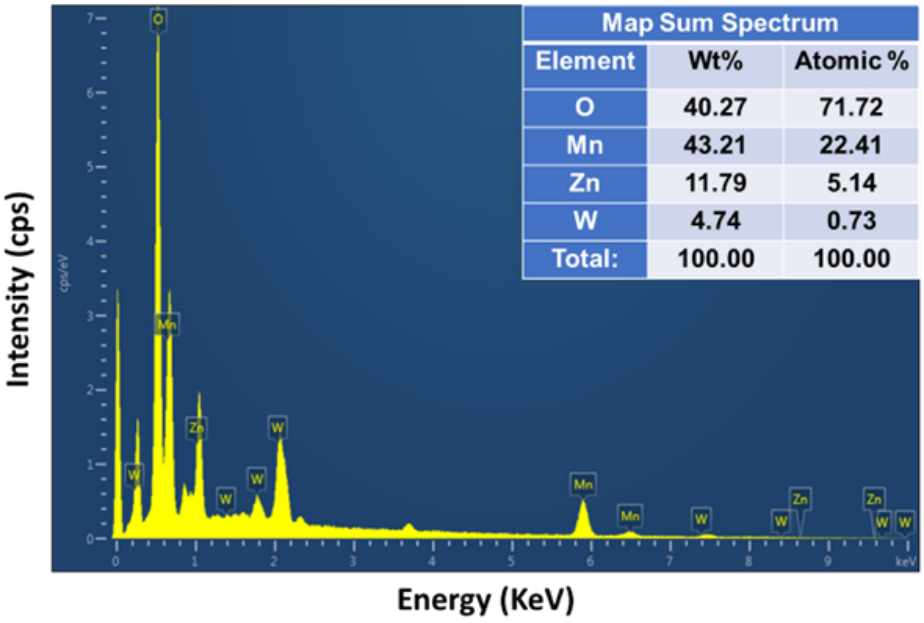

Figure S62. FE-SEM-EDX spectrum of the used $Zn_{0.1}Mn_{0.9}WO_4$/NF electrode indicating the presence of Zn, Mn, W, and O after a 24 h CA test at 1.0 V (vs. Hg/HgO).

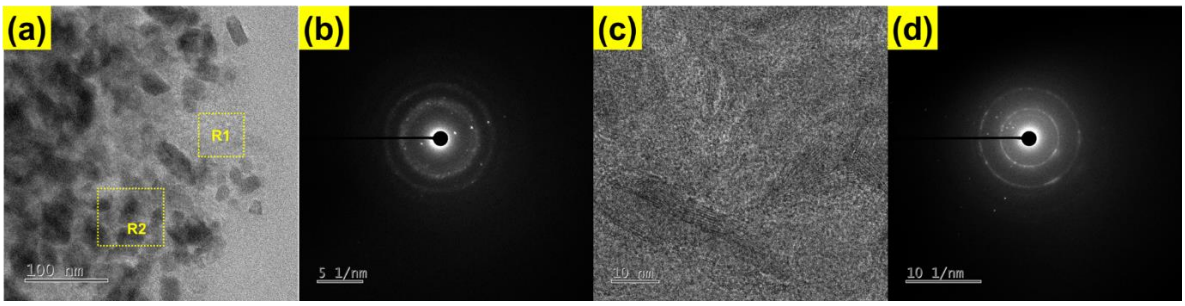

Figure S63. Post-catalytic TEM image and SAED pattern of the sample isolated from the used $Zn_{0.1}Mn_{0.9}WO_4$/NF electrode after 24 h CA at an applied potential of 1.0 V (vs. Hg/HgO).

Table S8. Quantitative analysis of the TEM-EDX spectrum of $Zn_{0.1}Mn_{0.9}WO_4$

Element	(keV)	Mass%	Atom%
O K (Ref.)	0.525	37.95	81.60
Mn K	5.894	13.45	8.42
Zn K	8.630	2.61	1.37
W M	1.774	45.99	8.61
Total		100.00	100.00

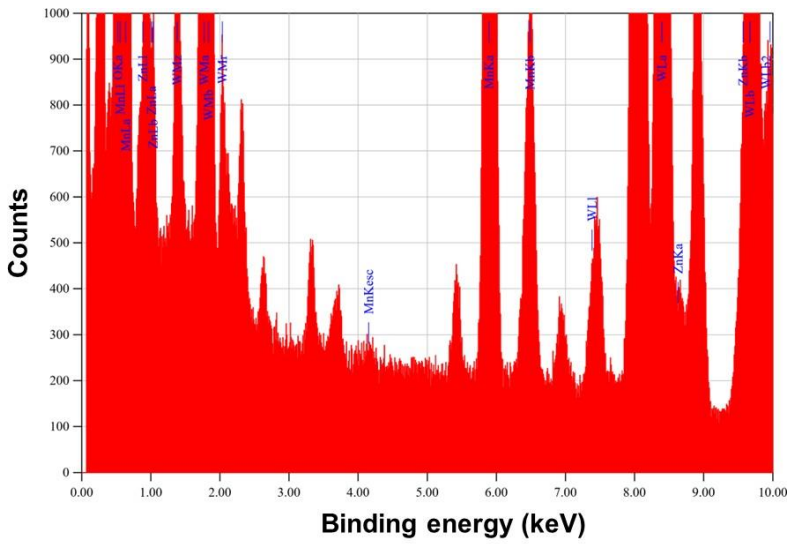

Figure S64. TEM-EDX spectrum of the sample isolated from the used $Zn_{0.1}Mn_{0.9}WO_4$/NF electrode after 24 h chronoamperometry test at 1.0 V (vs. Hg/HgO).

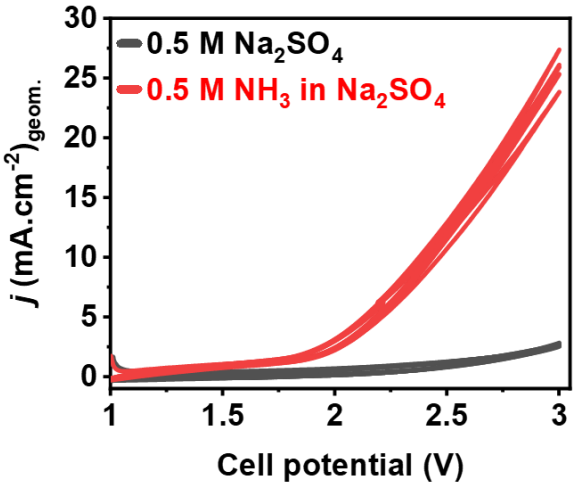

Figure S65. Cyclic voltammetric curves recorded in a two-electrode cell with interelectrode separation of 1 cm in presence of NH_3 in the electrolyte and in absence of NH_3 using $Zn_{0.1}Mn_{0.9}WO_4$/NF as an anode.

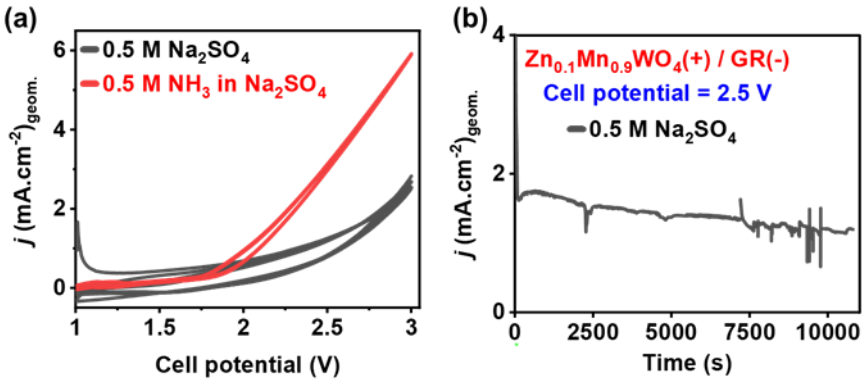

Figure S66. (a) Cyclic voltammetric curves recorded in a two-electrode cell in Hoffman apparatus (inverted burette cell set-up) with inter-electrode separation of approximately 8 cm. (b) CA curve for 3 h bulk electrolysis in 0.5 M Na_2SO_4 only using $Zn_{0.1}Mn_{0.9}WO_4$/NF(+)/(-) graphite rod (GR).

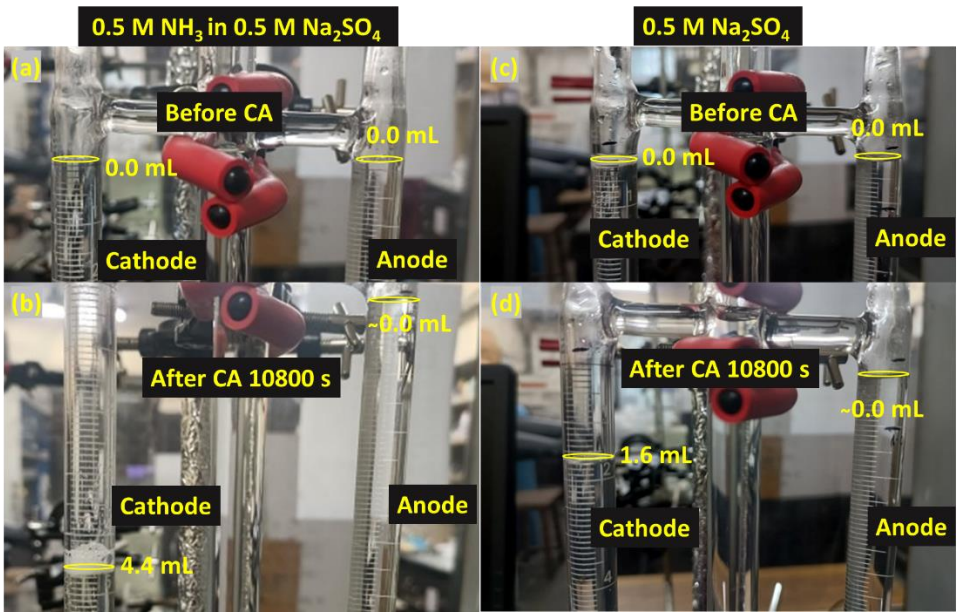

Figure S67. Picture of the two-electrode cell in Hoffman apparatus, marking on the solvent front (a) before and (b) after bulk electrolysis using 0.5 M NH_3 in 0.5 M Na_2SO_4 as electrolyte. Note: A minimal amount of gas evolved in the anode chamber, whereas 4.4 mL H_2 was found to be the only product in the cathode chamber. (c) Before and (d) after the bulk electrolysis in 0.5 M Na_2SO_4 electrolyte (only 1.6 mL H_2 was formed at the same applied potential in the cathodic chamber).

References.

(1) Adak, M. K.; Basak, H. K.; Kumar, S.; Chakraborty, B. Detection of a Nickel-Oxide Nanolayer During Mild Acid Treatment of Nickel Foam and Its Effect on Alkaline Oxygen Evolution and Ammonia Oxidation Reactions. *ACS Appl. Nano Mater.* **2024**, *7*, 8329-8340.
(2) Perdew, J. P.; Burke, K.; Ernzerhof, M. Generalized Gradient Approximation Made Simple. *Phys. Rev. Lett.* **1996**, *77*, 3865-3868.
(3) Anisimov, V. I.; Zaanen, J.; Andersen, O. K. Band theory and Mott insulators: Hubbard U instead of Stoner I. *Phys. Rev. B* **1991**, *44*, 943-954.
(4) Kresse, G.; Hafner, J. Ab initio molecular-dynamics simulation of the liquid-metal--amorphous-semiconductor transition in germanium. *Phys. Rev. B* **1994**, *49*, 14251-14269.
(5) Kresse, G.; Joubert, D. From ultrasoft pseudopotentials to the projector augmented-wave method. *Phys. Rev. B* **1999**, *59*, 1758-1775.
(6) Kresse, G.; Furthmüller, J. Efficient iterative schemes for ab initio total-energy calculations using a plane-wave basis set. *Phys. Rev. B* **1996**, *54*, 11169-11186.
(7) Monkhorst, H. J.; Pack, J. D. Special points for Brillouin-zone integrations. *Phys. Rev. B* **1976**, *13*, 5188-5192.
(8) Ganose, A. M.; Jackson, A. J.; Scanlon, D. O. sumo: Command-line tools for plotting and analysis of periodic* ab initio* calculations. *J. Open Source Softw.* **2018**, *3*, 717.
(9) Kirklin, S.; Saal, J. E.; Meredig, B.; Thompson, A.; Doak, J. W.; Aykol, M.; Rühl, S.; Wolverton, C. The Open Quantum Materials Database (OQMD): assessing the accuracy of DFT formation energies. *npj Comput Mater* **2015**, *1*, 15010.
(10) Mancheva, M. N.; Iordanova, R. S.; Klissurski, D. G.; Tyuliev, G. T.; Kunev, B. N. Direct Mechanochemical Synthesis of Nanocrystalline $NiWO_4$. *J. Phys. Chem. C* **2007**, *111*, 1101-1104.
(11) Tong, W.; Li, L.; Hu, W.; Yan, T.; Guan, X.; Li, G. Kinetic Control of $MnWO_4$ Nanoparticles for Tailored Structural Properties. *J. Phys. Chem. C* **2010**, *114*, 15298-15305.
(12) Phan, V. T. T.; Nguyen, Q. P.; Wang, B.; Burgess, I. J. Electrocatalytic Oxidation of Ammonia to Nitrate Occurs on NiOOH with OH/O Vacancies. *J. Am. Chem. Soc.* **2025**, *147*, 10758-10771.

(13) Liu, H.; Yang, C.-J.; Dong, C.-L.; Wang, J.; Zhang, X.; Lyalin, A.; Taketsugu, T.; Chen, Z.; Guan, D.; Xu, X.; et al. Electrocatalytic Ammonia Oxidation to Nitrite and Nitrate with NiOOH-Ni. *Adv. Energy Mater.* **2024**, *14*, 2401675.
(14) Vu, T. M.; Johnston, S.; Simondson, D.; Nguyen, C. K.; Nguyen, T. D.; Zeil, D. V.; Hocking, R. K.; Macfarlane, D. R.; Simonov, A. N. High-Rate, High-Selectivity Electrochemical Oxidation of Ammonia to Nitrite with a Silver-Based Catalyst. *ACS Catal.* **2024**, *14*, 10974-10986.
(15) Basak, H. K.; Adak, M. K.; Rajput, A.; Chakraborty, B. Low Pt Loading on Wolframite-Type $NiWO_4$ to Excel the Electrocatalytic Water Splitting and Ammonia Oxidation Reaction. *ACS Appl. Mater. Interfaces* **2025**, *17*, 9391-9406.
(16) Cohen, S.; Johnston, S.; Nguyen, C. K.; Nguyen, T. D.; Hoogeveen, D. A.; Van Zeil, D.; Giddey, S.; Simonov, A. N.; MacFarlane, D. R. A CoO_xH_y/β-NiOOH electrocatalyst for robust ammonia oxidation to nitrite and nitrate. *Green Chem.* **2023**, *25*, 7157-7165.
(17) Medvedev, J. J.; Tobolovskaya, Y.; Medvedeva, X. V.; Tatarchuk, S. W.; Li, F.; Klinkova, A. Pathways of ammonia electrooxidation on nickel hydroxide anodes and an alternative route towards recycled fertilizers. *Green Chem.* **2022**, *24*, 1578-1589.
(18) Yang, X.; Sun, L.; Liu, X.; Yang, Z.; Sun, H.; Liu, W.; Chen, H. Vacancy-Driven Ammonia Electrooxidation Reaction on the Nanosized CeO_x Electrode in Nonaqueous Electrolyte. *ACS Catal.* **2024**, *14*, 6236-6246.
(19) Nagita, K.; Yuhara, Y.; Fujii, K.; Katayama, Y.; Nakayama, M. Ni- and Cu-co-Intercalated Layered Manganese Oxide for Highly Efficient Electro-Oxidation of Ammonia Selective to Nitrogen. *ACS Appl. Mater. Interfaces* **2021**, *13*, 28098-28107.
(20) Huang, J.; Cai, J.; Wang, J. Nanostructured Wire-in-Plate Electrocatalyst for High-Durability Production of Hydrogen and Nitrogen from Alkaline Ammonia Solution. *ACS Appl. Energy Mater.* **2020**, *3*, 4108-4113.
(21) Tsai, M.-H.; Chen, T.-C.; Juang, Y.; Hua, L.-C.; Huang, C. High catalytic performance of CuCo/nickel foam electrode for ammonia electrooxidation. *Electrochem. commun.* **2020**, *121*, 106875.
(22) Johnston, S.; Cohen, S.; Nguyen, C. K.; Dinh, K. N.; Nguyen, T. D.; Giddey, S.; Munnings, C.; Simonov, A. N.; MacFarlane, D. R. A Survey of Catalytic Materials for Ammonia Electrooxidation to Nitrite and Nitrate. *ChemSusChem* **2022**, *15*, e202200614.
(23) Katayama, Y.; Okanishi, T.; Muroyama, H.; Matsui, T.; Eguchi, K. Electrochemical Oxidation of Ammonia over Rare Earth Oxide Modified Platinum Catalysts. *J. Phys. Chem. C* **2015**, *119*, 9134-9141.
(24) Johnston, S.; Kemp, L.; Turay, B.; Simonov, A. N.; Suryanto, B. H. R.; MacFarlane, D. R. Copper-Catalyzed Electrosynthesis of Nitrite and Nitrate from Ammonia: Tuning the Selectivity via an Interplay Between Homogeneous and Heterogeneous Catalysis. *ChemSusChem* **2021**, *14*, 4793-4801.
(25) Xiao, Z.; Huang, Y.-C.; Dong, C.-L.; Xie, C.; Liu, Z.; Du, S.; Chen, W.; Yan, D.; Tao, L.; Shu, Z.; et al. Operando Identification of the Dynamic Behavior of Oxygen Vacancy-Rich Co_3O_4 for Oxygen Evolution Reaction. *J. Am. Chem. Soc.* **2020**, *142*, 12087-12095.
(26) Liu, H.-Y.; Lant, H. M. C.; Troiano, J. L.; Hu, G.; Mercado, B. Q.; Crabtree, R. H.; Brudvig, G. W. Electrocatalytic, Homogeneous Ammonia Oxidation in Water to Nitrate and Nitrite with a Copper Complex. *J. Am. Chem. Soc.* **2022**, *144*, 8449-8453.
(27) Li, L.; Tang, C.; Yao, D.; Zheng, Y.; Qiao, S.-Z. Electrochemical Nitrogen Reduction: Identification and Elimination of Contamination in Electrolyte. *ACS Energy Lett.* **2019**, *4*, 2111-2116.
(28) Harmon, N. J.; Rooney, C. L.; Tao, Z.; Shang, B.; Raychaudhuri, N.; Choi, C.; Li, H.; Wang, H. Intrinsic Catalytic Activity of Carbon Nanotubes for Electrochemical Nitrate Reduction. *ACS Catal.* **2022**, *12*, 9135-9142.
(29) Sahana, T.; Valappil, A. K.; Amma, A. S. P. R.; Kundu, S. NO Generation from Nitrite at Zinc(II): Role of Thiol Persulfidation in the Presence of Sulfane Sulfur. *ACS Org. Inorg. Au* **2023**, *3*, 246-253.